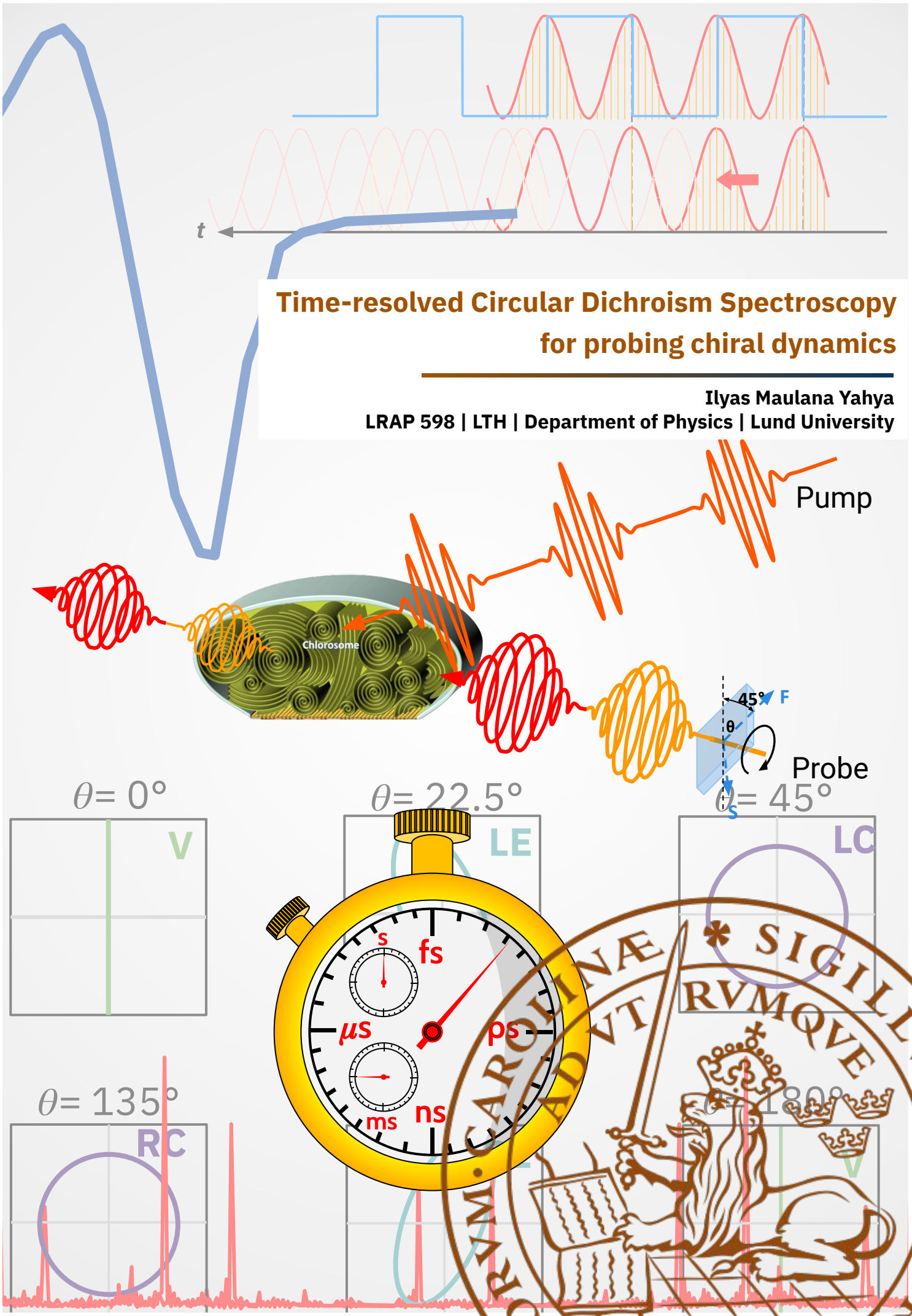
t
Time-resolved Circular Dichroism Spectroscopy
for probing chiral dynamics
Ilyas Maulana Yahya
LRAP 598 | LTH | Department of Physics | Lund University
Pump
Chlorosome
45°
F
θ
Probe
θ= 0°
V
θ= 22.5°
LE
θ= 45°
LC
s
fs
μs
ps
ms
ns
θ= 135°
RC
θ= 180°
V

Time-resolved Circular Dichroism Spectroscopy for Probing Chiral Dynamics

LUNDS UNIVERSITET

MASTER THESIS IN PHYSICS

by Ilyas Maulana Yahya

Supervisor: Donatas Zigmantas
Co-Supervisor: Cord Arnold
Examiner: Lars Rippe
LRAP: 598

A thesis submitted for the degree of Master in Photonics at Lund University

Division of Chemical Physics
Department of Chemistry, Lund University
Lund, Sweden 2024

Abstract

Time-resolved Circular Dichroism Spectroscopy for Probing Chiral Dynamics

Ilyas Maulana Yahya

Chirality can be understood as a property of an object that cannot be superimposed on its mirror image, such as our left and right hands. It is ubiquitous in nature and can also be found in the photosynthesis process involving chlorosomes from green sulfur bacteria. Understanding the dynamics of chiral properties in chlorosomes, due to the excitons formed by the interaction between bacteriochlorophyll c from green sulfur bacteria, could lead to a breakthrough in designing systems or devices that mimic its functionality to provide clean and sustainable energy solutions. One way to achieve this is to build Time-Resolved Circular Dichroism (TRCD) Spectroscopy. This technique is based on the different absorption of left- and right-polarized probe pulses by the chiral material after being excited by the pump beam.

In this project, a TRCD is build by utilizing a motor-driven rotating quarter wave plate to modify the existing two-dimensional electronic spectroscopy (2DES) setup, to achieve alternating right- and left-circularly polarization of the probe pulses. Synchronization of the motor-driven rotating quarter wave plate to the 2DES system, optimization and test measurements of the TRCD setup were conducted. We demonstrate that the developed TRCD setup has sufficient capability to probe the chiral properties of an molecular antenna in photosynthetic bacteria, containing aggregates of bacteriochlorophyll c molecules. Thus, this work opens new avenues to explore transient dynamics in chiral materials and observe changes in chiral symmetry on a femtosecond timescale.

Acknowledgements

In the Name of Allah—the Most Compassionate, Most Merciful.

So surely, with hardship comes ease. Surely with that hardship comes more ease.
- Qur'an 94:5-6 (Surah Ash-Sharh)

Firstly, Alhamdulillahirabbil'alamin. La hawla wala quwwata illa billah. I would like to express the enourmous amount and countless grateful and gratitudeness to Allah subhanahu wata'ala. He is the King of the King that without Him, I am nobody, without Him I would not exist in this world, without Him everything I did would not been possible to happen. All praises be to Allah, The God of the entire universe no one before Him and no one after Him.

Secondly, I would like to express my gratitude and gratefulness to Donatas whom firstly introduce this super-exciting topic. I also want to thankful of his constant guidance, superintensive support during the work of the project and many insightful discussion about optics, lasers, laser industries, good-practice in handling optics and many more. I, definitely, will remember when act as a research in the field of laser spectroscopy. I would like to thankful and grateful to have Cord as my teacher whom already give me guidance and support in many cases from the beginning of my Master in Photonics program since I came here for the first ever my lifetime to Sweden about two years ago. Thank you Roman, Egle, Edo, and Chandni for the help during my stay in Chemical Physics. Thank you very much Ramunas for the contribution to setup the new camera and the measurement program. Thank you also Jens for letting me brought your power meter system and thermally adhesive epoxy within those simple contribution the TRCD setup will be not be accomplished. Thank you also to Arthur for the programming part of the software. Thank you also to Dmitry for the guidance in wet lab introduction and the risk assesments. Thank you for all friends along with my study here in Lund to, Jinke, Samuel, Xinze, Andrea, Emelie, Joseph, Paul, and Jiayang. With out cheerful discussion out from studies and lectures, there are no international engagements. Thank you also for Indonesian students in Scania that also gives many outdoor activities.

I also want to thankful, grateful, and express my gratitude to Indonesian Endowment Funds for Education or LPDP for giving me a chance and fund my study here in Lund University in Master Photonics's program. Finally, I really want to thankful, grateful, express my great gratitude to my wife Maryam and my daugther Hanin for unbelievable and continuous supports and understandings for two years accompanying me to study. I really love them so much as a love my parents. Thus, I also want to thankful, grateful, express my great gratitude to my mother, father, brother and sisters and family in laws in Indonesia for the encouragement to maintain my spirit to continue study abroad and to pursue one of my dreams.

Popular Science Summary

In nature, one can often find symmetry, particularly handedness symmetry referred to as chirality. Think of chirality as an object that does not match its mirror image, similar to how our left and right hands are mirror images but cannot be superimposed on each other. This concept extends to molecules, with amino acids being a prime example. Almost all of the 22 essential amino acids are left-handed, or left-enantiomers, and their mirror images are called enantiomers.

The necessity of understanding the presence of selective chirality in nature provides a motivation to explore mechanisms underlying chirality. Also a big part of chemistry, biochemistry and pharmaceutics rely on asymmetric synthesis (of selective enantiomers) and catalysis. New findings in these research fields would give essential understanding to have better efficacy of pharmaceutical synthesis with fewer side effects, and also could be used to understand the fundamental and intricate molecular mechanisms in the photosynthesis processes. These processes often involve chlorophyll-type molecules, which are for example building blocks of chlorosome, that has chiral properties due to its molecular structural geometry. The goal is to learn from the natural self-assembling and self-repairing photosynthetic systems how to efficiently convert sunlight to chemical energy and try to design systems or devices that mimic this functionality, to provide clean and sustainable energy for the future generations. To further this understanding, scientists utilize a method known as circular dichroism spectroscopy. Circular dichroism relies on the observation that chiral molecules interact differently with light that can twist—either to the right (clockwise) or to the left (counter-clockwise). When this twisted light passes through chiral molecules, light with different handedness is absorbed differently. This differential absorption helps scientists to study the unique properties of these molecules.

Typically, circular dichroism provides only a steady state information, similar to taking a photograph, which shows what these molecules look like in their ground state but not how they change over time when excited by light. To capture these rapid changes, especially those occurring in femtoseconds—a quadrillionth of a second—researchers are developing advanced techniques such as time-resolved circular dichroism spectroscopy. Such techniques will allow them to create movie-like sequences of molecular motion, revealing how excited chiral molecules dance and interact in time. Such detailed observation is pivotal for harnessing the secrets of nature's processes and could lead to groundbreaking technologies in energy conversion and medicine. The main aim of this project was to build and test a novel TRCD spectroscopy setup by using a synchronously rotating quarter wave plate to provide an alternating right- and left-circular polarization of the probe pulse. The setup was tested on the photosynthetic antenna chlorosome featuring excitonic transitions sustained by the huge aggregates of bacteriochlorophyll molecules.

Contents

1 Introduction

Circular dichroism is a fascinating phenomenon that involves the way certain molecules interact with light. It involves a different amount of absorption of the twisted light-either right or left circularly polarized light by the chiral molecules. Understanding this property would help scientists to reveal sophisticated mechanism in the photosynthetic process to convert sunlight to chemical energy and try to design a system that imitate this functionality, to provide clean and sustainable energy for future generations.

Circular dichroism (CD) spectroscopy is a well-established technique used in structural biology to elucidate the secondary structure of biomolecules in solution [1]. By differentially absorbing left- and right-circularly polarized light, CD spectroscopy offers valuable insights into the chiral properties of molecules. In physical phenomena studies, CD spectroscopy is often employed to explore spin-polarized states of the materials, where transitions between different spin states lead to selective absorbtion of either right or left circularly polarized light. Time-resolved circular dichroism (TRCD) spectroscopy further advances this field by combining ultrafast pump-probe spectroscopy's high temporal resolution with CD spectroscopy's structural sensitivity, enabling for example the investigation of biomolecular conformational dynamics on ultrafast timescales [1]. Here the system is first excited by the linear polarized light promoting the system to the excited state, which are then probed with circularly polarized light, thus the chiral properties of the excited states are probed.

In recent years, TRCD spectroscopy has witnessed significant excitement, leading to attempts to achieve a deeper understanding of biomolecular behavior and function. For instance, Mitchell [2] employed first principles modeling and TRCD spectroscopy to study the Fenna-Matthews-Olson (FMO) complex, shedding light on its conformational dynamics and demonstrating TRCD spectroscopy's potential in biomolecule analysis.

Changenet-Barret and Hache [1] reviewed recent breakthroughs in ultrafast TRCD spectroscopy, discussing challenges and opportunities in developing CD measurements to the time domain. They emphasized the importance of recent developments in laser technologies and non-linear optics, opening new possibilities for TRCD spectroscopy in studying ultrafast chirality changes in biological systems and beyond.

1.1 Objective

While the literature abounds with studies on TRCD spectroscopy [3–9], the current work aims to contribute to this field by providing an alternative way to build and develop

TRCD setup by utilizing a motor-driven-rotating quarter wave plate (rot-QWP) and used to test the setup on the antenna complex chlorosome from photosynthetic green sulfur bacteria. By introducing the motor-driven-rotating quarter wave plate to an existing two-dimensional electronic spectroscopy (2DES) setup at the division of Chemical Physics in Lund, we aim to detect TRCD signals without any polarization artifacts signal. This thesis provides an analysis of the construction, calibration, and evaluation of the TRCD using motor-driven-rotating quarter wave plate.

Three challenges were posed to achieved this goal: (i) to design, build, and incorporate the motor-driven rotating quarter wave plate to the existing 2DES and synchronize with the rest of the setup, (ii) to calibrate, and (iii) to test the TRCD spectroscopy setup to measure the TRCD signal of the chlorosome.

1.2 Motivation

Attempts to build and develop TRCD spectroscopy have been ongoing since the early 1970s [1]. Until the 20th century, TRCD remained too rudimentary to be widely used in the scientific community. Nowadays, there are two types of TRCD: ellipsometric TRCD and direct-TRCD. Ellipsometric TRCD relies on unchanged polarization states of the probe pulses interacting with a chiral sample, resulting in polarization changes that are decomposed using polarizing optical elements to retrieve the CD signal through Jones calculus.

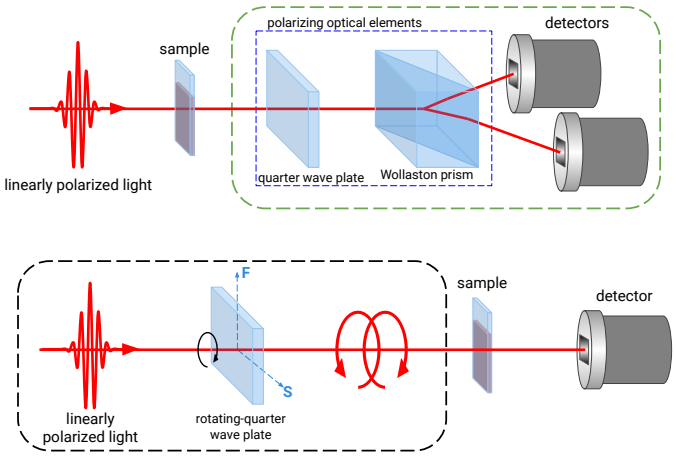

Figure 1.1: The difference between ellipsometric and direct TRCD. In an ellipsometric TRCD (top), the polarizing optical elements and detectors (green box with dashed line) can be configured in various ways depending on how the polarization after propagating through the sample is decomposed. In contrast, direct TRCD (bottom) focuses on changing the polarization state of light before it interacts with the sample. The polarizing optical elements (inside the black box with dashed line) can also vary depending on the specifications of the time-resolved setup in a particular lab. Note that the linear polarized light can be either horizontally or vertically polarized.

For example, Changenet and Hache (2023) built an ellipsometric TRCD using a combination of a polarizer, chiral sample, quarter-wave plate, and Wollaston prism, combined with balanced detection [4] (see top of Fig. 1.1). In contrast, direct-TRCD is based on

the fact that the probe pulses' polarization state needs to alternate between left-circularly polarized (LCP) and right-circularly polarized (RCP) (or vice versa) before interacting with the sample, without additional polarizing elements before the detector. An example of this type is by Ress et al., who used a polarization grating to change the polarization state of the probe pulses [10].

Recalling from the extensive research about TRCD [1–9], there are two types of TRCD measurements with its general advantages and disadvantages which are summarized in the Table 1.1.

Table 1.1: Two types of time-resolved circular dichroism spectroscopic measurements with its advantages and disadvantages.

Aspects	Ellipsometry tr-CD	Direct tr-CD
Principles	Elliptically polarized probe beams. It relies on the circular dichroism of the sample [2].	Different absorption of right- and left-circularly polarized light due to intrinsic circular dichroism of the system, by utilizing, often a photo-elastic modulator (PEM) and phase-locked detection [1].
Pros and Cons	Enabling detection of extremely small signals [2], but prone to polarization artifacts, e.g. optical rotatory dispersion (ORD), circular birefringence (CB), linear dichroism (LD), and linear birefringence (LB) [2], due to cross-polarization detection scheme, and therefore, required low birefringence cells with low stress on their window, and more complex data analysis [1].	Strong achiral background absorption which is typically in the order of $10^{-6} - 10^{-4}$, decreasing the signal-to-noise ratio (SNR) and an inherent scattering background from the sample, further limiting the SNR ratio [1].

However, it is worth to note that both measurement techniques also experience the same artifacts as steady-state measurements, whereas photoexcitation can cause additional artifacts signals [1]. In addition, the modulation of probe pulses from linearly to circularly polarized or variable phase delay on the linearly polarized probe require sequential acquisition procedures, i.e. time-consuming, and prone to pulse-to-pulse fluctuations, decreasing the signal-to-noise ratio [1]. Several research groups have attempted to develop and improve, either the ellipsometric or direct TRCD. For example, Stadnytskyi et al., has performed a 3-channel optical detection scheme and data processing protocol, enabling ordinary absorption and CD simultaneously, approaches shot-noise limit, relatively fast signal integration time, and can measure as small as 20 μdeg [11]. Moreover,

Changenet and Hache (2023) have successfully achieved artifact-free TRCD spectroscopy and improved signal-to-noise ratio with very short acquisition times by employing balanced detection geometry using a combination of quarter wave plate and Wollaston prism without modulating any polarization state [4].

On the other hand, the notable improvement of direct TRCD was achieved by Oppermann et al., by using 50 kHz PEM coupled to fast reading-out dispersive detection with dual-array CMOS detector, resulting in accuracy about 10 μOD[1] (<1 mdeg). Nevertheless, it requires complex electronics synchronization to extract the TRCD signal from six consecutive probe pulses [5]. Furthermore, Morgenroth et al., has successfully achieved multifilament supercontinuum femtosecond pulses while still maintaining its circularly polarization state. They employed a BBO Pockels cells to switch the polarization state of 400 nm pulses between left- or right-circularly polarized which is then used as a seed pulse [12]. In the following two years, they have been improving the previous design by replacing the BBO with deuterated KDP (DKDP) crystal Pockels cells, resulting in higher time resolution to 100 fs, higher intensity of the circularly polarized multifilament supercontinuum light and lower intensity fluctuations [13]. Recently, Ress et al., performed direct TRCD, utilizing polarization grating as its key element, without requiring active electronic polarization-modulating devices [10].

All above developments and improvements have their specific benefits and drawbacks which are depend on the experimental configuration that has been employed and extensive review on both methods can be found elsewhere [1]. In spite of previous developments and improvements in the artifact reduction, sensitivity of measurement, broadband measurements and reasonable good time resolution, none of the methods have reached a level, where they would provide reliable information in the TRCD studies. Thus there is still a demand for the new TRCD methods. Our method relies on modifying the high SNR two-dimensional electronic spectroscopy (2DES) setup with a motor-driven-rotating quarter wave plate and using only two laser beams, instead of four that are used in the 2DES experiment. The motivation for attempting building such a TRCD setup are as follows:

1. Augulis and Zigmantas (2011) have demonstrated two-dimensional electronic spectroscopy with double modulation lock-in detection [14]. The technique eliminated artifacts or "ghost" signals in 2D spectra arising from scattering and accumulation of long-lived species [14]. This can be extended to develop TRCD measurement to provide a relatively high signal-to-noise ratio.

2. Paleček and Zigmantas introduced a double-crossed polarization transient grating for the distinction and characterization of superposition of states (coherence). The study presented a technique that can be implemented in TRCD setups to eliminate artifacts or "ghost" signals arising from scattering and accumulation of long-lived species [15]. This, again, can be used to provide a high sensitivity signal of TRCD.

By modifying the existing 2DES setup developed from the aforementioned references and inserting motor-driven rotating quarter wave plate (rot-QWP) to modulate the polarization

[1] OD stands for optical density that is mainly used by chemist while physicist defined it in degree

state of the probe pulses, one could obtain alternating left- and right-circularly polarized probe pulses that are differently absorbed by chiral materials after being excited by the pump beam, i.e. a direct TRCD spectroscopic method, as shown in Fig. 1.2. This novel setup not only holds a promise for artifact reduction, high sensitivity, broadband and high time resolution, but also can serve as a pathway to develop two-dimensional circular dichroism spectroscopy (2DCD), a long sought spectroscopic technique. Moreover, the advantage of this development is threefold, i.e. the change in polarization is twice faster than the rotation frequency of the device, decoupling from the fundamental harmonic. Furthermore it allows for a flexibility to switch between different time-resolved techniques with relative ease. For example, as in this project, pump-probe (or transient absorption)[2] and TRCD spectroscopy. It can be very convenient to have many types of spectroscopic tools in one table-top setup, and a relatively high SNR ratio.

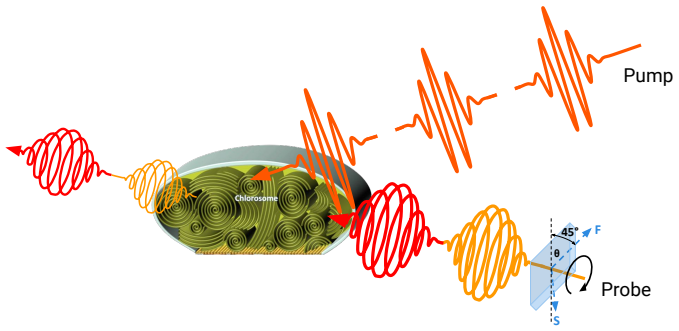

Figure 1.2: An illustration of the TRCD spectroscopy idea in this project. The pump beam is chopped and the probe beam is polarization-modulated by rotating quarter wave plate.

1.3 Thesis outline and scope of this work

The theoretical framework for the project is provided in Chapter 2, covering a summary of polarization optics, circular dichroism, and optical and laser spectroscopy, with special emphasise on the concepts relevant to this work. Chapter 3 covers a detailed explanation of the experimental methods as well as how to design, build, calibrate and test the setup in the laboratory. In Chapter 4, the most important results of the work are collected and a discussion of them is presented. The thesis concludes with Chapter 5, where a general assessment of the work is made as well as a reflection on possible future steps. This project is mainly experimental and technical work as the modelling and fitting of the measured time-resolved circular dichroism spectra and the dynamics would take substantial amount of time, and is out of the scope of the project.

[2]Shortly, pump-probe spectroscopy is a technique used to perturb atoms in a lattice out of their equilibrium with a first beam (pump) to excite the sample into excited states. Subsequently, a second beam (probe) "freezes," with a relative time delay τ, the atoms before they relax back to their equilibrium position with respect to the lattice. By repeating this measurement with different τ, one can reconstruct the full time dynamics of the atoms that are excited by the pump beam. Note that atoms in a lattice are chosen for a convenient example

2 | Theory

In this chapter, the theoretical background that is relevant to the main project will be discussed. Firstly, the brief and relevant concept and equations on polarization optics, starting from general representation of light polarization, matrix representation (also known as Jones calculus), polarization ellipse, until matrix representation of some optical components, will be provided. The subsequent section will focus on the optical phenomenon that underlies the heart of the project thesis, i.e. circular dichroism.

In addition to that, the concept of time-resolved spectroscopy, also called pump-probe spectroscopy, will be briefly described, with particular emphasis on the relevant physical concepts. The chapter will end with a description of the sample that is used.

2.1 Jones representations

The state of light can be described by its polarization state (for example of the electric field vector), since it contains the amplitude and phase of the light that propagates into optical systems. The simple approach to achieve this is, by considering the work from Robert Clark Jones, Jones calculus [16]. The main feature of this approach is to represent the polarization state of light and optical components by a vector and/or matrix, respectively, assuming that the light is fully polarized [16]. Several examples of the polarization state of light are shown in Tab. 2.1 below.

The general vector form of the polarization state of light can be describe as

$$\mathbf{J} = \begin{bmatrix} A_x \\ A_y \end{bmatrix}. \tag{2.1}$$

where $A_x = a_x \exp(i\varphi_x)$ and $A_y = a_y \exp(i\varphi_y)$ are the complex envelopes of the electric field in x and y components [16]. Substituting these complex envelopes to a monochromatic plane wave of frequency ν and angular frequency $\omega = 2\pi\nu$, travelling in z direction with velocity c, i.e.

$$\mathbf{E}(z,t) = \mathrm{Re}\left\{(A_x\hat{x} + A_y\hat{y}) \exp\left[i\omega\left(t - \frac{z}{c}\right)\right]\right\} \tag{2.2}$$

that yields

$$E_x = a_x \cos\left[\omega\left(t - \frac{z}{c}\right) + \varphi_x\right] \tag{2.3a}$$

$$E_y = a_y \cos\left[\omega\left(t - \frac{z}{c}\right) + \varphi_y\right]. \tag{2.3b}$$

Table 2.1: Several polarization state of light. Note that the definition of right-and left-circular polarization in this thesis is defined when the light propagate towards the observer.

LP at an angle	RCP	LCP
$\begin{bmatrix}\cos\theta \\ \sin\theta\end{bmatrix}$	$\frac{1}{\sqrt{2}}\begin{bmatrix}1 \\ i\end{bmatrix}$	$\frac{1}{\sqrt{2}}\begin{bmatrix}1 \\ -i\end{bmatrix}$

Combining the above equations, forms a polarization ellipse. The related parameters of such polarization ellipse are the ratio of the complex amplitude $R = a_y/a_x = |A_y|/|A_x|$ and the phase difference $\varphi = \varphi_y - \varphi_x = \arg\{A_y\} - \arg\{A_x\}$. Hereupon, the polarization ellipse can be characterized by two parameters, namely, ellipticity χ and angle ψ. The ellipticity angle χ is calculated from the ratio of the minor to major axes of the ellipse b/a and the angle ψ is the direction of major axis [16], both of them are related to the ratio of complex amplitude R and the phase difference φ, viz.

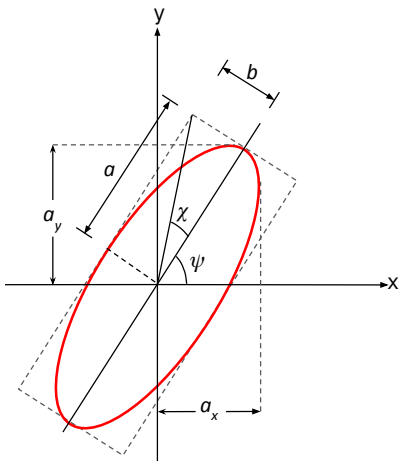

Figure 2.1: The polarization ellipse with its parameters. Image inspired by [16].

$$\tan 2\psi = \frac{2R}{1 - R^2}\cos\varphi \tag{2.4a}$$

$$\sin 2\chi = \frac{2R}{1 + R^2}\sin\varphi. \tag{2.4b}$$

Fig. 2.1 shows all the parameters of the polarization ellipse.

2.1.1 Matrix of the optical systems

The prior discussion was mainly about the polarization state of light represented by Jones vector. However, an optical elements or system, such as a linear polarizer, mirror, wave plate and combination of them, can be represent by a Jones matrix, akin of ABCD matrix for ray optics. Its origin is based on the fact that the calculation can be considered as a linear systems, thus linear algebra can be performed, to obtain the Jones matrix that corresponds to a specific optical elements or systems that are mentioned before.

Now, think of a light with defined polarization state, e.g. $\mathbf{J}_2$, and a defined polarization state $\mathbf{J}_1$ after propagating through an optical element, then the matrix form can be written as [16]

$$\mathbf{J}_2 = \mathbf{T}\mathbf{J}_1 \quad \text{or} \quad \begin{bmatrix} A_{2x} \\ A_{2y} \end{bmatrix} = \begin{bmatrix} T_{11} & T_{12} \\ T_{21} & T_{22} \end{bmatrix} \begin{bmatrix} A_{1x} \\ A_{1y} \end{bmatrix} \tag{2.5}$$

where $\mathbf{T}$ is called the Jones matrix of an optical system or element. The matrix Eq. 2.5 shows that the Jones matrix $\mathbf{T}$ affects the Jones vector $\mathbf{J}_1$ to change its polarization state and intensity. Accordingly, one can construct an optical system with its corresponding Jones matrix as a cascaded Jones matrix, i.e.

$$\mathbf{J_f} = \mathbf{T}_n \cdots \mathbf{T}_3\mathbf{T}_2\mathbf{T}_1\mathbf{J_i} \tag{2.6}$$

where subscripts $\mathbf{f}$ and $\mathbf{i}$ denote final and initial, respectively. Jones matrices for three optical elements are provided in Tab. 2.2 below.

Table 2.2: Three example of Jones matrix along with its corresponding optical elements. Note that the LP in this case means linear polarizer.

LP (in x-axis)	QWP	Plane mirror
$\begin{bmatrix} 1 & 0 \\ 0 & 0 \end{bmatrix}$	$\begin{bmatrix} 1 & 0 \\ 0 & -i \end{bmatrix}$	$\begin{bmatrix} 1 & 0 \\ 0 & 1 \end{bmatrix}$

Beside that, there is also another important Jones matrix that is useful to deal with rotating optical elements, as in this thesis, i.e. rotating QWP. This Jones matrix is corresponds to the coordinate transformation and is written as:

$$\mathbf{R}(\theta) = \begin{bmatrix} \cos\theta & \sin\theta \\ -\sin\theta & \cos\theta \end{bmatrix}. \tag{2.7}$$

The rotation can be defined as

$$\mathbf{T}^{'} = \mathbf{R}(\theta)\mathbf{T}\mathbf{R}(-\theta) \tag{2.8a}$$

$$\mathbf{T} = \mathbf{R}(-\theta)\mathbf{T}^{'}\mathbf{R}(\theta). \tag{2.8b}$$

All above equations from Eq. 2.6- 2.8 with Tab. 2.2 and Eq. 2.3 in Sec. 2.1 will be used to simulate the resulting polarization state of laser pulses after propagating through a rotating quarter wave plate and polarization ellipse analysis in 2DES setup in a subsequent paragraph.

Simulation of rotating quarter wave plate The simple schematic of the optical system for simulating the polarization state changes of laser pulse through a rotating quarter wave plate (QWP) is shown in Fig. 2.2. One should consider that in this case, for simplifications, the laser pulse is monochromatic and vertically linearly polarized light propagates through a rotating QWP without encountering pulse elongation due to material dispersion, which inherently existing the QWP. Therefore, the Jones vector and matrix for the laser pulse and rotating QWP can be describe as

$$\mathbf{J_{fqwp}} = \mathbf{QWP^{rot}J_V} = \mathbf{R}(\theta)\,\mathbf{QWP}\,\mathbf{R}(-\theta)\mathbf{J_V} \tag{2.9}$$

where $\mathbf{J_{fqwp}}$, $\mathbf{QWP^{rot}}$, $\mathbf{J_V}$ and $\mathbf{R}(\theta)$ are the final Jones vector after propagating through a rotating QWP, a rotating QWP, the intial Jones vector for vertically linearly polarized light, and the coordinate transformation matrix, respectively. Inserting all related equations from Sec. 2.1.1 and 2.1 and applied it in Matlab (the matlab code is provided in the Appendix A.1), gives the result that is shown in Fig. 2.3.

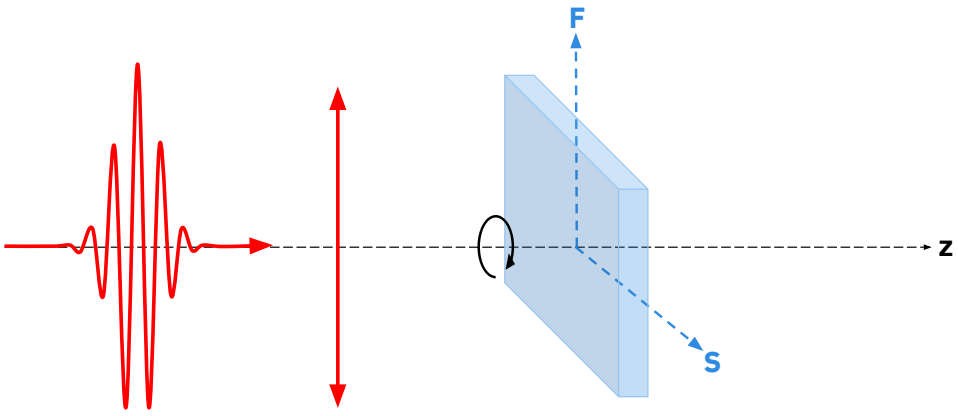

Figure 2.2: The schematic of the laser pulse propagating through rotating quarter wave plate. Note that the circular arrow denotes the rotation for the simulation only and it is not related to the actual case in the setup (the actual rotating is in the opposite direction). The z-axis correspond to the direction of propagation of the laser pulses, F (y-axis) correspond to fast axis, and S (x-axis)correspond to the slow axis of the quarter wave plate

The Fig. 2.3 shows that the polarization state of the laser pulses, indeed, changes from vertical to circular and goes back to vertical again. The interesting feature from the optical systems in Fig. 2.2 is that, the elliptically polarized laser pulse is oriented only in y-axis, denoting that the contribution from the polarization along x-axis is completely zero which is obvious from the fact that the incoming polarization state is vertically linearly polarized. Furthermore, the polarization ellipse at 45° and 135° shows a direct relation between the

rotation direction of the QWP to the orientation of the circular polarization of light. This result shows that by rotating a QWP, one can change the polarization state of laser pulses, alternating from vertical to either LCP or RCP in order to perform selective absorption of LCP and RCP laser pulses, i.e. circular dichroism.

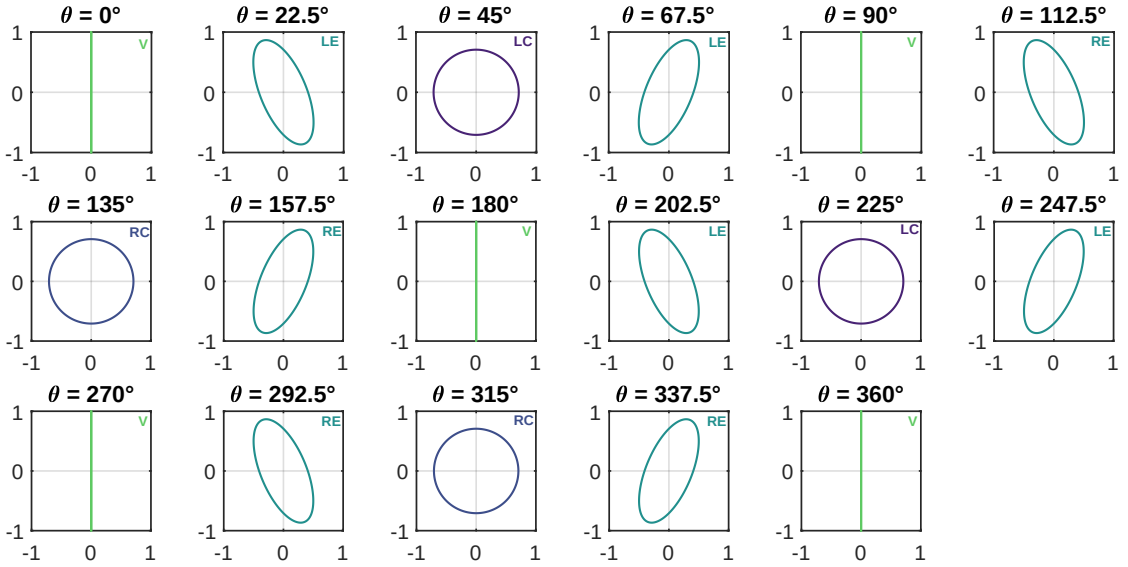

Figure 2.3: The resulting polarization ellipse from the optical systems in Fig. 2.2. V=vertical polarized, LE=left elliptical, LC=left circular, RE=right elliptical, RC=right circular. In addition, the horizontal and vertical axis is the E_x and E_y, respectively. Moreover, one should keep in mind that the direction of the laser pulse propagation is going out from the polarization ellipse or going toward a reader.

Polarization ellipse analysis of 2DES setup In order to simulate and anaylze the polarization ellipse in 2DES setup, there are approximations that need to be kept in mind, i.e. the polarization state changes from RCP to LCP after reflected by the spherical mirrors. The schematic that is used to simulate the polarization ellipse is shown in Fig. 2.4. The Jones matrices that are considered is started after the beam splitter, i.e. RR1, M1, rot-QWP, M2, M3, SM1, M4, SM2, and a linear polarizer in x-axis (LPx) or at 0°. The reason for choosing these optical components is that the polarization state changes happen along all of these optical components. It was also assumed that the SM2 give additional 5° off since this spherical mirror is directed slightly down with respect to the propagation direction.

Let's now turn into the Jones matrices for the optical system. All the Jones matrices for QWP, LPx and rotation matrix have been provided in Tab. 2.2 and Eq. 2.7. However, there is a difference for the plane mirror in Tab. 2.2 when circularly polarized light propagates towards it. For instance, when left circularly polarized light is reflected with a plane mirror and spherical mirror, it becomes right circularly polarized light. This means that the second diagonal component is negative. Additionally, the retroreflector has negative one in all of its diagonal components. Therefore, the complete Jones matrices are written

as

$$\mathbf{J_f = LPx^{rot}\, SM_2^{rot}\, M_4\, SM_1\, M_3\, M_2\, QWP^{rot}\, M_1\, RR_1\, J_V}. \tag{2.10}$$

By inserting the corresponding Jones matrices (the details are available in the Appendix A.2), the resulting polarization ellipse directly after the SM2 and the transmitted intensity after LPx is shown in Fig. 2.5.

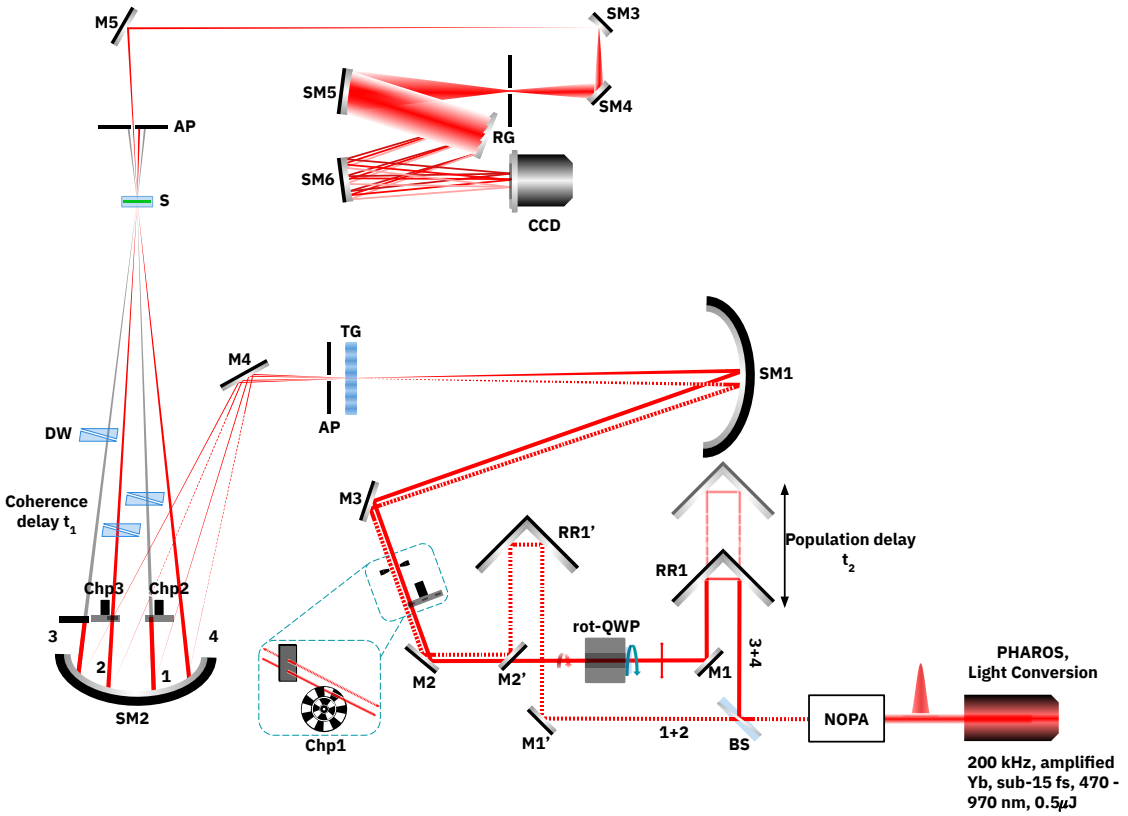

Figure 2.4: The simplified scheme of the modified 2DES setup. The acronyms are NOPA: non-linear optical parametric amplifier, BS: non-polarizing beam splitter, M: mirror, RR: retroreflector, rot-QWP: rotating quarter wave plate, SM: spherical mirror, TG: transmission grating, Chp: chopper, AP: aperture, DW: double wedges, S: sample, RG: relfection grating, CCD: charge coupled device. Note that the 1 and 2 beams path in the setup is indicated by dots, meaning that the beams 1-2 is on top of the beams 3 and local oscillator. The 1st and 3rd beam (grey color) is blocked when TRCD is performed. Moreover, for the simulation purpose, these blocked beams are not considered and only one beam is used for the simulation, i.e. the 4th beam.

Based on the simulation result, it is obvious that the polarization ellipse is circularly polarized light when the QWP is directed at an angle of 45° and the transmitted intensity, when the LPx is directed at the same angle as for the QWP, behaves sinusiodally. Furthermore, this simulation result also shows that all above assumption can be used to mimic the real condition in the 2DES setup. Moreover, the additional 5° off does not alter the polarization ellipse after it reflected by SM2, its only rotates the polarization state by a factor of 5°, thus, the polarization state is still circular polarization as shown in right Fig. 2.5. Thereupon, this simulation result can be used as complementary check for the synchronization between the triggered pulses that dictates the rotary stage's rotation and

the polarization stage changes of the laser pulses.

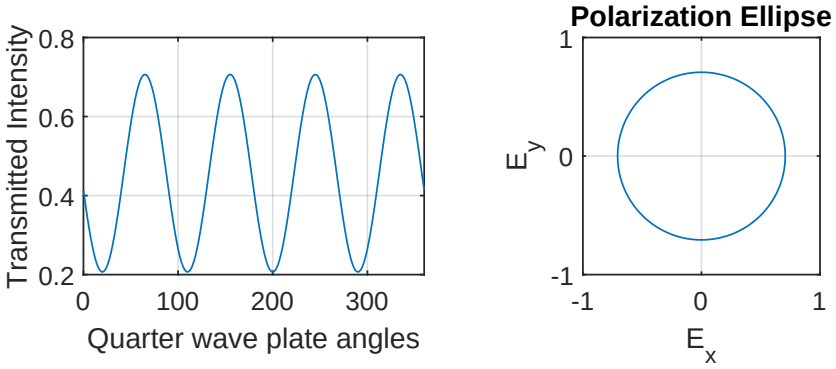

Figure 2.5: The simulation result of transmitted intensity in 2DES setup based on Eq. 2.10 when the linear polarizer at a constant angle 45° (left) and its corresponding polarization ellipse after the SM2 and before LPx at 45° (right). It should be note that the transmitted intensity, indeed, as a result from rotating QWP at different angles whereas the polarization ellipse on the right is only shows on particular angle of the rotating QWP, i.e. 45°.

2.2 Circular dichroism

Understanding circular dichroism can be described by chiral light as one concept and the chiral property of the material as the second, i.e. circularly polarized light and circular dichroism, respectively.

2.2.1 Circularly polarized light

Eq. 2.2 is a solution of Maxwell's equations in form of a plane-wave solution that can be written also as

$$\mathbf{E}(\mathbf{r},t) = \mathbf{A}_0 \exp\left[i\left(\mathbf{k}.\mathbf{r} - \omega t\right)\right] \tag{2.11}$$

where $\mathbf{k}$ and $\mathbf{r}$ is now in a general form, i.e. the wave vector in three dimensions. The specific waves that propagate along the $\hat{z}$ axis and the polarization lies in the xy-plane with arbitrary phase, then the Eq. 2.11 becomes Eq. 2.3.

Table 2.3: The corresponding parameters in polarization ellipse for vertically linearly polarized and circularly polarized light (CPL). Note that the sign (+)RCP (−)LCP follows the similar definition in Tab. 2.1.

Pol. state	a_x , a_y	φ	E_x , E_y
LP	$a_x \neq 0, a_y \neq 0,$ $a_x \neq a_y$	$n\pi$ for $n = 0, \pm1, \pm2, \ldots$	$E_y = \pm(a_y/a_x)E_x$
CPL	$a_x = a_y$	$n\pi/2$ for $n = \pm1, \pm3, \ldots$	$E_x^2 + E_y^2 = a_0^2$

Using the parameters in polarization ellipse in Fig. 2.1, one can analyze the corresponding circularly polarized plane wave from its magnitude and phase. This is summarized in

Tab. 2.3. Based on Tab. 2.3, when the $\varphi = n\pi$ for $n = 0, \pm1, \pm2, \ldots$ and $a_x = a_y$, the x- and y- components oscillates either in phase or out of phase. This creates a both electric-field in x- and y- components oscillates along a line at an angle $\tan^{-1}(E_y/E_x)$ with relation between E_y and E_x is a straight line with a slope of a_y/a_x. On the other hand, when the magnitude is still the same, $a_x = a_y$, nevertheless the phase is $\varphi = n\pi$ for $n = \pm1, \pm3, \ldots$, then the polarization is circular, due to the magnitude relation of $E_x^2 + E_y^2 = a_0^2$. This yields to the circular polarized plane wave, based on Eq. 2.11, that can be written as

$$\mathbf{E}(z,t) = \mathbf{A}_0 \left[\hat{\mathbf{x}} + \exp(\pm i\pi/2)\hat{\mathbf{y}}\right] \tag{2.12a}$$

$$\mathbf{E}(z,t) = \mathbf{A}_0 \left[cos\left(kz - \omega t\right)\hat{\mathbf{x}} \mp sin\left(kz - \omega t\right)\hat{\mathbf{y}}\right]. \tag{2.12b}$$

2.2.2 Absorption coefficient

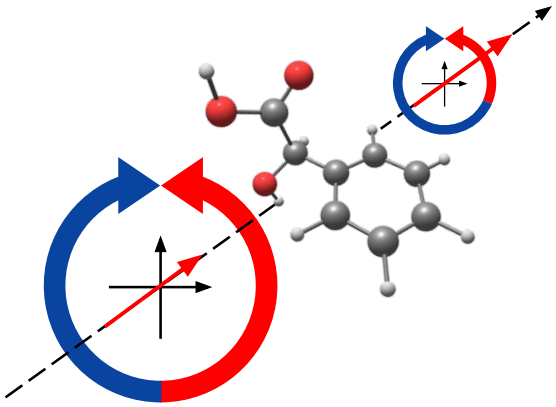

Figure 2.6: The schematic circular dichroism. Note that the blue and red arrow indicates the LCP and RCP, respectively. Image inspired from [17].

The absorption of a medium can be describe by Beer-Lambert law which is defined as

$$\frac{\delta l}{l} = -\ln(10)\,\varepsilon\, C\,\delta z \text{ or } A(\lambda) = \varepsilon(\lambda)Cl = -\log\left(\frac{I(\lambda)}{I_0(\lambda)}\right) \tag{2.13}$$

where ε is the absorption coefficient, C is the concentration, δz is the thickness of a thin layer of sample, on which that light illuminate the sample at the normal incidence, l and δl is the intensity of the incoming light and the reduced intensity due to absorption after propagate through the sample. One can write the absorption coefficient[1] as

$$\varepsilon = \frac{N_A}{2303}\frac{w}{l} \tag{2.14}$$

[1] δl is equal to the number of molecules in the layer, δN, times w, the average absorbed per molecule per second , $\delta l = w\delta N$. If the unit of concentration is moles per liter, $\delta N = (NC/1000)\delta z$ because l is defined in terms of unit cross-sectional area

where N_A and w is the Avogadro's number and the average energy absorbed per molecule per second. From this, circular dichroism can be defined [18]

$$\Delta\varepsilon = \varepsilon_- - \varepsilon_+ = \frac{N_A}{2303}\frac{w_- - w_+}{l} \tag{2.15}$$

where subscripts + and − denote the absorption of RCP and LCP, respectively. Additionally, there is also another practical form of circular dichroism that is commonly uses in standard steady-state circular dichroism spectroscopy which is [1]

$$CD = \Delta\varepsilon \cdot l \cdot c = (\varepsilon_- - \varepsilon_+) \cdot l \cdot c. \tag{2.16}$$

In general, CD is a tiny effect, typically in the order of 10^{-3} or 10^{-4} compare to the absorption coefficients [19] and the unit for CD is the same as absorption, i.e. optical density (OD)[2].

2.3 Optical and laser spectroscopy

The following sections provide the description of nonlinear optics, an underlying concept for the optical parametric amplification (OPA) and nonlinear spectroscopy, as particular example is the pump-probe. This is followed by the explanation of heterodyne-detected transient grating.

2.3.1 Nonlinear optics

Nonlinear optics in frequency domain When an electric field is applied to a dielectric material, it generates a macroscopic electric dipole moment called polarization $\boldsymbol{P}(\omega)$[3]. When week field is applied the induced polarization exhibits a linear dependence on the electric field, $\boldsymbol{E}(\omega)$ which can be written as [16]

$$\boldsymbol{P}(\omega) = \varepsilon_0 \left[\boldsymbol{\chi}(\omega) \cdot \boldsymbol{E}(\omega)\right] \tag{2.17}$$

where the $\boldsymbol{\chi}(\omega)$ is the optical susceptibility of the material and ω is the angular frequency. The term polarization $\boldsymbol{P}(\omega)$ can acts as a source of radiation at certain frequency ω. In principle, all the optical properties of material and its corresponding phenomena such as absorption, refraction, reflection, scattering, etc. are associated with $\boldsymbol{P}(\omega)$ as defined in Eq. 2.17. The polarization oscillates at the same frequency as the incoming electric field. However, in general, when the incoming electric field has large intensity the χ itself depends on electric field and the polarization can be expressed as

$$\boldsymbol{P} = \boldsymbol{P}^L + \boldsymbol{P}^{NL} = \varepsilon_0 \left[\boldsymbol{\chi}^{(1)} \cdot \boldsymbol{E} + \boldsymbol{\chi}^{(2)} \cdot \boldsymbol{E}^2 + \boldsymbol{\chi}^{(3)} \cdot \boldsymbol{E}^3 + \cdots + \boldsymbol{\chi}^{(N)} \cdot \boldsymbol{E}^N\right]. \tag{2.18}$$

[2] it is often to write a unit of CD also in deg or mdeg, i.e. mili degree [10]
[3] bold symbols denote vectors or tensors

$\chi^{(1)}$ is the linear optical susceptibility and correspond to the susceptibility at low intensity, $\chi^{(2)}$ is the second-order nonlinear optical susceptibility and is a third rank tensor containing 27 elements, which correspond to the possible combinations of the three Cartesian components of the polarization and of the two interacting electric fields, $\chi^{(3)}$ is the third-order nonlinear optical susceptibility and is a fourth rank tensor with 3^4 elements [16], and $\chi^{(N)}$ is the high-order nonlinear optical susceptibility. The nonlinear susceptibility is only relevant, if the electric field is strong[4] and the material itself has an inversion symmetry (centrosymmetric media) for exhibiting $\chi^{(3)}$ or lack of inversion symmetry (non-centrosymmetric media) for exhibiting $\chi^{(2)}$.

Non-collinear optical parametric amplification (NOPA) Having a broadband spectrum is beneficial for pump-probe spectroscopy, and it will define the achievable temporal resolution of the experiment. Many spectroscopists utilize the non-collinear optical parametric amplification (NOPA) to generate broadband laser pulses. NOPA is a three-wave mixing process or second-order nonlinear effect that involves three waves, as is clear from the name. The basic idea is to amplify wavelengths of interest by utilizing nonlinear crystals. In the present case Beta Barium Borate (BBO), that serves as the device for amplification. Mainly, the NOPA consist of the pump beam ω_p, signal beam ω_s and idler beam ω_i (see left Fig. 2.7).

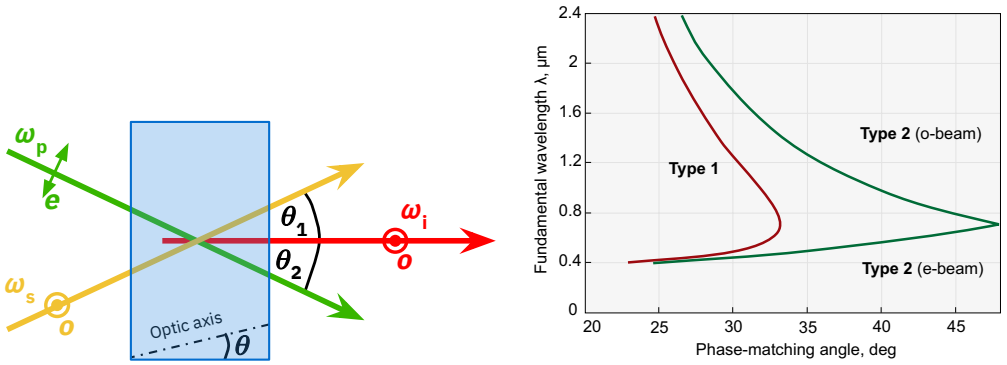

Figure 2.7: The type-I phase matching geometry of non-collinear optical parametric amplification (left) in BBO crystal. Note that the color-coded arrow represent the second harmonic from the output of Yb:KGW laser (green solid line), the white light generation from YAG crystal (seed, yellow solid line), and the sum-frequency generation (red solid line). The phase matching angle as a function of wavelength, or the so-called tuning curves, of type-I and II (right). The left image is inspired from Ref. [16] while the right image was taken from EKSMA Optics, UAB.

Basically, when the pump beam ω_p comes at an angle, having horizontal polarization, as well as the signal beam ω_s, having vertical polarization, with respect to the normal surface of the nonlinear crystal, due to the birefringent properties of the crystal, i.e. has polarization-dependent refractive index, the pump and signal beam will experience different refractive index. The pump beam provides the required energy for the coherent

[4] the order of magnitude of the elements of $\chi^{(1)}$ is 1, $\chi^{(2)}$ is $10^{-24} - 10^{-21}$m/V for a typical dielectric crystals, semiconductors, and organic materials and $\chi^{(3)}$ is $10^{-34} - 10^{-29}$m/V for a typical glasses, crystals, semiconductors, and organic materials [16].

amplification to amplify the signal and generate the idler beam. Moreover, in order to interact efficiently, they must be phase-matched, i.e. pump and signal beam, by tuning the angle of the birefringent crystal. The gain of the amplified signal beam depends on the power of the pump beam [16]. There is a certain phase-matching angle, which corresponds to certain wavelength range that one can amplify, this can be determined from the so-called tuning curves as shown in right Fig. 2.7.

Nonlinear optics in the time domain The Eq. 2.17 and 2.18 above can be written down in the time domain:

$$\boldsymbol{P}(t) = \int_{\infty}^{+\infty} \boldsymbol{\chi}\left(t - t'\right) \boldsymbol{E}\left(t'\right) dt' \tag{2.19}$$

and

$$\boldsymbol{P}(t) = \boldsymbol{P}^{(1)}(t) + \boldsymbol{P}^{(2)}(t) + \boldsymbol{P}^{(3)}(t) + \cdots . \tag{2.20}$$

The expression in the first term can be written in the other form as

$$\boldsymbol{P}^{(1)}(t) = \int_{0}^{\infty} dt_1 S^{(1)}(t_1) \boldsymbol{E}(t - t_1) \tag{2.21}$$

where the $S^{(1)}(t_1)$ is the linear response function in the time domain, similar to the linear optical susceptibility $\chi^{(1)}$ in the frequency domain. Analogous to the linear response function, the third-order nonlinear response function can also be deduced from the third-order nonlinear polarization which is written as [19]

$$\boldsymbol{P}^{(3)}(t) = \int_{0}^{\infty} dt_3 \int_{0}^{\infty} dt_2 \int_{0}^{\infty} dt_1 S^{(3)}(t_3, t_2, t_1) \boldsymbol{E}(t - t_3) \boldsymbol{E}(t - t_3 - t_2) \boldsymbol{E}(t - t_3 - t_2 - t_1) \tag{2.22}$$

where the $S^{(3)}(t_3, t_2, t_1)$ is the third-order nonlinear response function[5]. Eq. 2.21 and 2.22, in fact, are the convolutions of the response function and the external field functions and this response function contains all the information about the optical properties of the systems as well as in Eq. 2.18. This equation also serves as a basic for any nonlinear spectroscopy technique that is based on third-order polarization, such as pump-probe spectroscopy, as will be discussed below.

2.3.2 Pump-probe spectroscopy

In order to clearly observed a dynamic change of a rapidly moving horse or a racing car, one can use high-speed electronic cameras to catch many frames in one second, resulting in many images. Similar approach to this is also found in measuring ultrafast dynamics processes that happen in chemical reaction and solid-state materials. To achieve and resolved the ultrafast processes one needs to use an ultrashort laser pulses to "freeze" the ultrafast movement within the object of interest. The most common experimental technique

[5] the expression of the third-order nonlinear response function and its significancy can be found detail in Ref. [19, 20]

that physicists and chemists use is pump-probe. The main idea could be understood as follows and by looking at Fig. 2.8[6]; a first short pulse, called **pump**, arrives impinging on the atoms in a lattice and excites dynamics, inducing the atoms to move along the lattice axes. After some delay τ, relative to the pump pulse, a second pulse is arriving at the same atoms in the lattice, called a **probe**. This combination of two pulses is used to follow the dynamic processes that are triggered by the pump pulse. Essentially, by repeating a series of different time delays τ, one can reconstruct the full time dependence of the dynamic changes in the material response [21]. Furthermore, one can relate measurement results to a microscopic model of the corresponding physical or chemical processes to obtain an insight of the dynamical processes that happen in the sample [21].

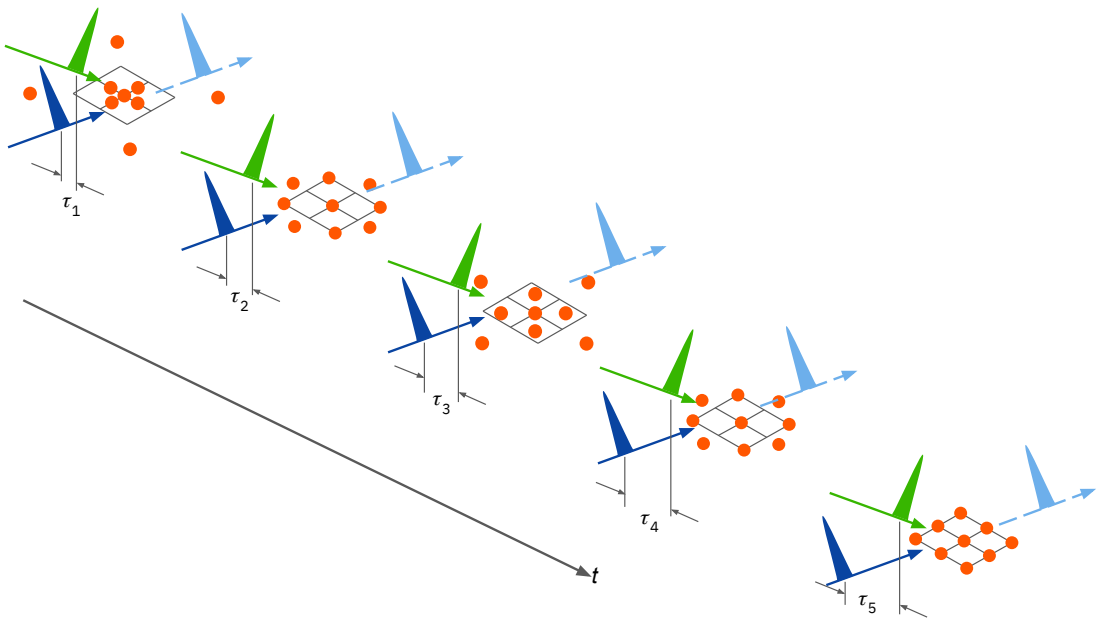

Figure 2.8: Time sequenced illustration of pump-probe scheme. The orange solid circles illustrate atoms in a lattice. Due to perturbation from the pump pulse, the atoms can move along the lattice axis. The time delay τ between pump and probe pulses is varied such that it capture the dynamic change of the atoms. Essentially, at τ_5, the atoms have nearly come backs to their equilibrium position in the lattice, when the probe pulses capture this moment.

As previously discussed in Sec.2.3.1, the pump-probe spectroscopy[7] is one example of nonlinear processes. Since, there are two pulses, i.e. pump and probe pulses, the radiation field that insert into Eq. 2.22 are the combination of both of the two given by [19]

$$\begin{aligned}\boldsymbol{E}(t') = \boldsymbol{E}_1\left(\boldsymbol{r}, t'+\tau\right)\left[\exp\left(i\boldsymbol{k}_1\cdot\boldsymbol{r} - i\omega_1 t'\right) + \exp\left(-i\boldsymbol{k}_1\cdot\boldsymbol{r} + i\omega_1 t'\right)\right] \\ + \boldsymbol{E}_2(t')\left[\exp\left(i\boldsymbol{k}_2\cdot\boldsymbol{r} - i\omega_2 t'\right) + \exp\left(-i\boldsymbol{k}_2\cdot\boldsymbol{r} + i\omega_2 t'\right)\right]\end{aligned} \tag{2.23}$$

where $E_j(t)$ is the temporal envelope and polarization of j-th pulse and τ is the delay between the two pulses as shown in Fig. 2.8. Both pump and probe pulses interact with the sample, and there will be any linear combination of the four individual wave vectors

[6] for convenience, atoms in a lattice is picked up as an example
[7] It is generally defined as transient absorption (TA) spectroscopy

and the similar combination of the four frequencies to consider, i.e.

$$(\pm\omega_1 \pm \omega_1 \pm \omega_2 \pm \omega_2) \tag{2.24}$$

and

$$(\pm\boldsymbol{k}_1 \pm \boldsymbol{k}_1 \pm \boldsymbol{k}_2 \pm \boldsymbol{k}_2). \tag{2.25}$$

However, signals of some of these combination will be averaged in the measurement (through the rotating wave approximation[8]) and the others will result in high-frequency oscillations that generates small and usually undetected contributions to the measured signal. The measured signal, in the experiment, can be directly determined by taking the absolute square of the emitted electric field, one can called it $\boldsymbol{E}_{\text{sig}}(t)$, which is proportional to the induced polarization $\boldsymbol{P}(t)$:

$$I_{\text{sig}} \propto |\boldsymbol{E}_{\text{sig}}(t)|^2 \propto |\boldsymbol{P}_{(t)}|^2. \tag{2.26}$$

This equation also called *homodyne* detection scheme which cannot detect the phase of the signal. The detection scheme that involves spectral interference between the emitted field with extra laser pulse can measure the signal phase and is called *heterodyne*[9].

2.3.3 Heterodyne-detected transient grating

The transient grating, more precisely, heterodyne-detection transient grating is one type of the third-order spectroscopies. The main idea is to send two temporally coincident pump pulses that are crossed at an angle and spatially overlap in a sample, generating a spatially modulated interference pattern, thus, also modulating the complex refractive index at the crossing region as shown in Fig. 2.9. The temporal dynamics of this modulated refractive index is probed by a third pulse, delayed by time τ, that is diffracted off into the Bragg angle and the intensity of this signal is, generally homodyne detected. However, in this case the real and imaginary parts of the complex third-order polarization cannot be determined separately and low amplitude contributions from the signal can be lost, hence, reducing the information of the data [23].

This can be eliminated by coherently mixing the weak signal $E_s(t)$ with a strong beam $E_{LO}(t)$, called local oscillator (LO) to enhanced the weak signal from the sample. The generated signal is then defined as [23]

$$I_T(t) = \frac{n(\omega)c}{4\pi} |E_{LO}(t) + E_s(t)|^2 = I_{LO}(t) + I_s(t) + 2\frac{n(\omega)c}{4\pi}\text{Re}\left[E^*_{LO}(t) \cdot E_s(t)\right] \tag{2.27}$$

where $n(\omega)$ and c is the refractive index of the sample and the speed of light, respectively. By utilizing, lock-in detection, the first term can be eliminated and the second term can

[8] It occurs since most cases the radiation has a frequency close to the resonance frequency at ω_0 thus the magnitude of detuning is small, i.e. $|\omega_0 - \omega| << \omega_0$ for further details see also Sec. 7.1.2 in Ref. [22] for comparison

[9] in four wave mixing technique e.g. transient grating and 2DES, they usually involve the local oscillator pulse that act as the 4th pulse

be neglected when $|E_s(t)| << |E_{LO}(t)|$. The third term is the combination between the LO and signal field, amplified by a factor of $2|E_{LO}(t)|/|E_s(t)|$, and thus an enhancement can be several orders or magnitude, depending on the relative amplitudes of the LO and signal fields. This detection type is sometimes called optical heterodyne detection (OHD). The third term can also be represented as

$$I_{OHD} \propto \mathrm{Re}\left[E^*_{LO}(t)E_s(t)\right] = \mathrm{Im}\left[E^*_{LO}(t)P^{(3)(t)}\right] = E_{LO}\cdot \mathrm{Im}\left[\exp(i\phi)P^{(3)}\right] \tag{2.28}$$

where ϕ is the phase difference between the signal and the LO field. In addition, the other advantage of OHD is that the real and imaginary parts of third-order polarization can be separated [23] by selectively controlling the LO in quadrature ($\phi = \pi/2, 3\pi/2, \cdots$) or in phase ($\phi = 0, \pi, \cdots$) with the signal field. Combining this with transient grating, one can have OHD-TG that can separate the real and imaginary parts of $P^{(3)}$. This means that, if the polarization state of the probe pulses is modulated, alternating from left- and right-circularly polarized, one can have optical heterodyne-detected transient grating circular dichroism (OHD-TGCD or for short TGCD) that can provide important information about the real and imaginary parts of $P^{(3)}$ which can reveal the transient circular dichroism feature of the sample. This can be achieved relatively conveniently in the existing 2DES setup (see Fig. 2.4) that has all the requirements to perform OHD-TGCD[10] (see Fig. 2.4), except that the coherence delay is not scanned compared to the 2DES.

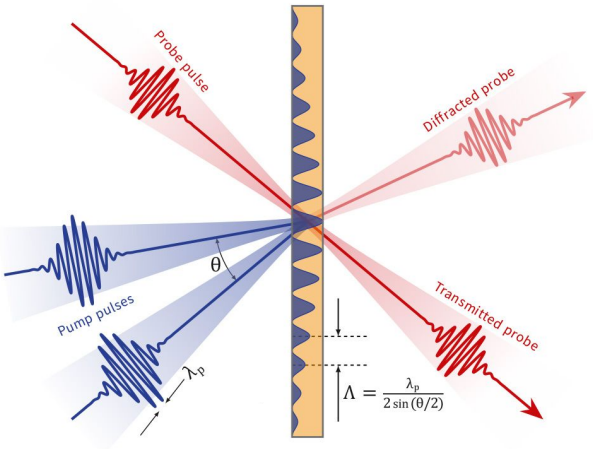

Figure 2.9: The principle of transient grating spectroscopy. The two pump pulses come with an angle with respect to each other at θ. They overlap spatially, creating a spatial interference pattern inside the sample. This figure is obtain from Light Conversion, Inc.

2.4 Chlorosome from green sulfur bacteria

Generally, green sulfur bacteria can be found in the sulfur-rich environment, such as the Black Sea, at a depth of up to 145 m. Quiet strikingly, it is also found in the coast

[10] in OHD-THG, it needs two beams to generate the transient grating. In Fig. 2.4 can be achieved by using beam 1 and 2 while the probe beam is the 3rd beam and the LO is the 4th beam

of Mexico at depth of 2.5 km where they live in a dim light from the black smokers, where no sunlight can reach them [24]. The structure of the photosynthetic unit (PSU) of green sulfur bacteria is shown in Fig. 2.10. The chlorosomes are the major unit of the light-harvesting pigments that efficiently capture the sunlight and transfer its energy in the form of molecular excitons to the reaction center, where this energy is converted into electrochemical energy used by bacteria. Chlorosomes are made up of many aggregates of *bacteriochlorophylls* (*BChls*) without the help of protein [25], creating supramolecular complexes that can form in a lamellae, tubes, and spirals [24]. Bacteriochlorophylls interact strongly in these aggregates, which results in delocalization of electronic states, which are described as molecular Frenkel excitons.

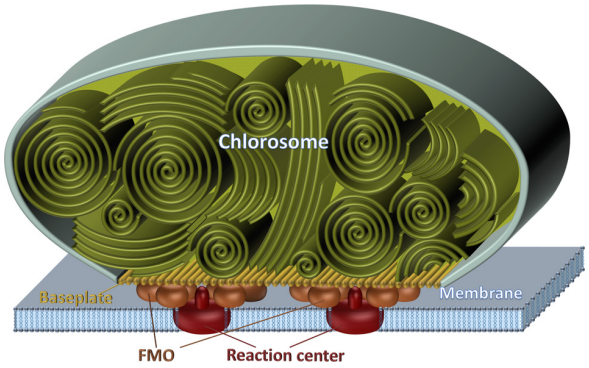

Figure 2.10: The photosynthetic unit (PSU) of green sulfur bacteria, consisting of chlorosome that contains bacteriochlorophyll *c*, *d* and *e*, Fenna-Matthews-Olson (FMO) complex and reaction center (left). The sample that was use in this project are isolated chlorosomes in the solution. The image was taken from Ref. [24].

As they act as the main light-harvesting unit for photosynthesis process, the energy transfer processes that take place on the timescale of few-hundred femtosecond to picosecond are highly important. Here we used the chlorosome from *Chlorobaculum tepidum* (*Chl. tepidum*) that has BChl *c*, shown in right Fig. 2.10 as the test object. Based on theoretical simulations, the relevant ultrafast dynamics in these systems are the exciton delocalization (100-200 fs) [26, 27], enery relaxation in the exciton manifolds ($\sim$ 50 fs) [24], relaxation process of four exciton states in the higer-lying state ($\sim$ 1 ps) [24], and relaxation among low-lying exciton states (between exciton levels that has different BChl layer of the chlorosomes lamellae) (10-20 ps) [24]. Apart from that, as the excitons formed by the interaction of BChl *c* feature optical transitions with chirality, they exhibit strong steady-state circular dichroism signal. It was found that the steady-state CD signal is around $\sim$380 mdeg [28] from one group and 1.6 mdeg [29] from the other group. An indication that the CD signal can vary dependent on the buffer solution and experimental settings, which are employed when measuring steady-state CD signal.

3 | Methods

The three challenges, described in 1.1, will be tackled by performing a number of tasks, which are described here. First, there is the mechanical/thermal management, programming, and electronic tasks, abbreviated for the sake of simplicity as mechatronics. This task is summarized in Section 3.1 and 3.2. The laser and optical tasks is provided in Section 3.3, and lastly the sample preparation task is given in Section 3.4.

The mechatronic task mainly relate to designing, building and adapting the current 2DES setup for the TRCD spectroscopy needs. This includes proper mounting of the quarter wave plate to the rotary stage, cooling of the rotor and the synchronization. The optical tasks focus on the alignment of the rotary stage in the existing 2DES setup and lock-in setup. Finally, the section closes with a description of the sample preparation that is used in this project.

3.1 Motor-driven rotating quarter-wave plate design and implementation

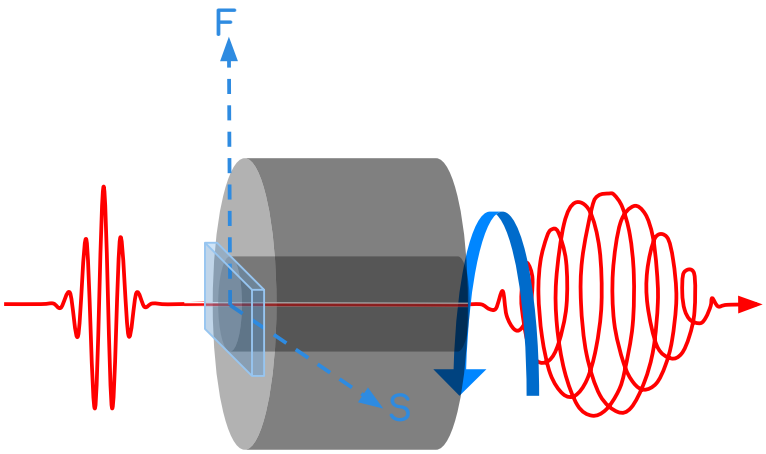

Figure 3.1: Schematic concept of the rotating quarter-wave plate. The quarter wave plate is attached to a modified mount in Fig. 3.2. It could be noted that the rotary stage (without the wave plate) does not affect the laser beam that propagates inside the hole. The circular arrow represents the actual rotation of the stage. Note also that all the axes that are defined in this schematic are similar to the one that is defined in Fig. 2.2.

The key component in our implementation of the direct TRCD spectroscopy is the quarter-wave plate that is attached to a rotary stage, having a small hole with diameter of 5 mm to let the probe pulses with modified polarization pass through the device. This is shown in Fig 3.1. When the incoming probe pulses go through the rotating quarter-wave plate, the linearly polarization of the probe pulses change gradually from linear to elliptical and from elliptical to circular, then back to elliptical and to linear. This sequence repeats many times as long as the rotary stage rotates. These alternating circularly polarized light can be used to probe the time-resolved chirality properties of the samples.

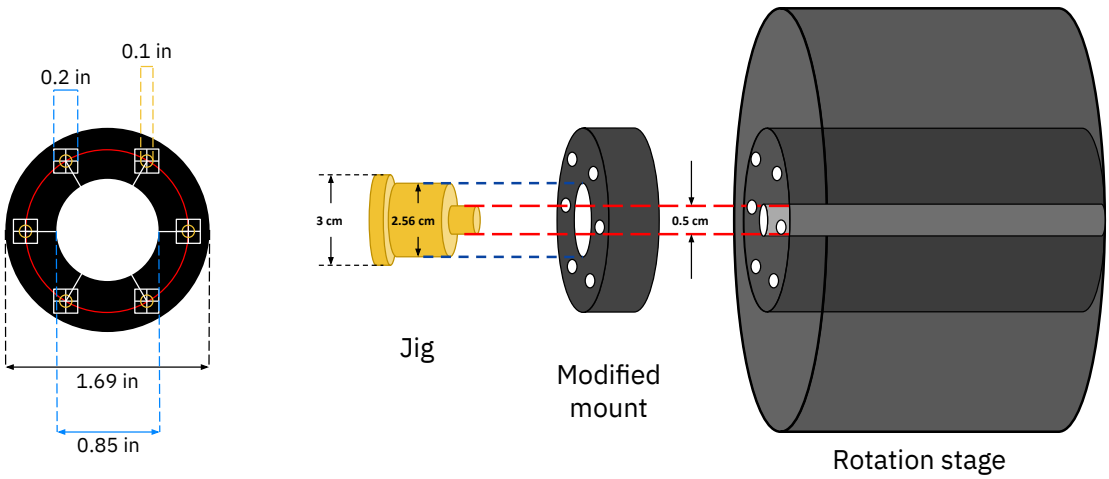

Figure 3.2: The design of the modified quarter wave plate mount to the rotary stage. The design template (left) is used to drill six holes that perfectly match to the six mounting holes of the rotary stage. The red circle is a guideline to ensure that the centers of the six holes perfectly coincide with the red circle.

The implementation of the concept from Fig. 3.1 is done by using 8MRL80 compact direct drive rotary stage, shortly rotary stage, from Standa, Ltd. which has a maximum velocity about 21600 deg/s or around 60 Hz and SPiiPlusCMnt rotary stage controller (ACS Motion Control Ltd.). The important step to mount the quarter wave plate is that to modified the OMR/M - RMS Microscope Objective Mount, M4 Tap from Thorlabs, Inc. to perfectly fit with the six threaded mounting holes in front of the rotary stage with the help of a dedicated special jig that is home-made.

The actual work was done as follows; the template guide was made at first with suitable diameter to match not only the thread hole in the wave plate mount but also with the diameter of the hole from the rotary stage, ensuring that the modified mount is centered to the rotary stage to minimize wobbling when it rotates rapidly. Subsequently, creating a six bolt holes in the mount to match the six bolt holes in the rotary stage. This is shown in the Fig. 3.2. The rotary stage is mounted on the custom made kinematic mount (from Liop-Tec) with two (x and y) adjusters.

Due to the rapid motion of the rotary stage, it was heating substantially and temperature measurement had to be performed. This temperature measurement was done to determine and build the appropriate liquid cooling system for the stage. The details of the

measurement and the water cooling system are provided in Appendix B.

3.2 Synchronization of rotary stage rotation

The successful steps in Sec. 3.1 would result in perfect rotation of the modified mount. To ensure this, preliminary rotation tests were done by performing configuration and initialization between the controller and the rotary stage to synchronize with the laser repetition rate using a pulse generator (DG535 from Standford Research Systems), which is triggered by the trigger signal from the laser. As a start, we focus on experimental setup needed to synchronize all the components in the setup, which is illustrated in Fig. 3.3.

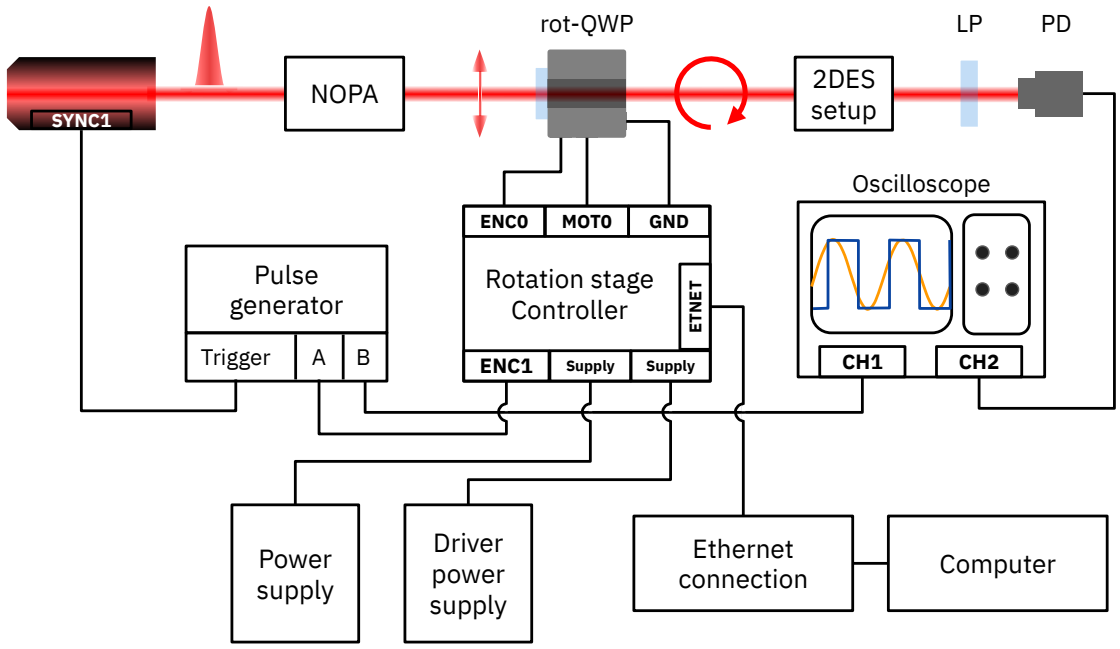

Figure 3.3: The simplified synchronization setup and the 2DES setup is shown in Fig. 2.4. Note that for synchronization purposes, the liquid cooling system describe in Appendix B.2 is not necessary to be installed. However, it is preferable to install it first before synchronizing the rotation of the rotary stage to ensure that the rotary stage has stable temperature, such that it does not affect the quarter wave plate, for example cause its bending.

Shortly, NOPA generates spectrally broad 660 - 820 nm pulses, which are compressed using a prism compressor. Upon arrival at the setup the pulses have vertically linear polarization, which then propagates through the rotating quarter wave plate, which induces modulation of light polarization. These laser pulses propagate through the linear polarizer and are detected by a photodiode which is connected to the oscilloscope. The laser sync signal is triggering the pulse generator (Fig. 3.3). The generator sends the TTL[1] level signal to the encoder of the rotary stage controller. Subsequently, the controller synchronizes the rotation of the stage with the generator signal. This is done by a simple script written in the controller software (see Appendix C.1). The synchronization step will be elaborated bellow.

[1] transistor-to-transistor logic. Logic 0 means that the voltage is zero and logic 1 means 5 V.

3.2.1 The pulse generator

As stated previously, the pulse generator is triggered by the laser pulse repetition rate (shortly rep rate). The standard laser rep rate used in the laboratory is 200 kHz, but the pulse picker installed in the laser is used to reduced this rate by 17 times, so the actual rep rate used in this project is 11765 Hz. The parameters in the pulse generator were set such that the synchronized pulse generator to the laser rep rate was approximately 57 Hz.

3.2.2 Validation of the rotation synchronization to the rest of the setup

By performing steps in 3.2.1 and C.1, one should validate the synchronization. The basic idea of the synchronization is to maintain a stable frequency of the rotation and stable phase among all the components — namely, the motor-driven chopper, rotary stage, and the CCD read-out — in the setup, as shown in Fig. 2.4and 3.3, by utilizing a pulse generator that sends synchronization signal to all these components. In other words, all elements of the setup have to be locked in synchronization.

3.3 Spectroscopy setup

3.3.1 Time-resolved spectroscopy setup

The direct TRCD spectroscopy setup used in this thesis is based on a modified 2DES setup. In the pump-probe (or transient absorption, TA) and TRCD implementation only two out of four beams are used, i.e. beam 2 and 4 (or LO), while beam 1 and 3 is blocked (see Fig. 2.4). However, in the case of heterodyne-detected transient grating circular dichroism (TGCD), all four beams were used[2] in a boxcars geometry (see Fig. 3.4)[3]. Briefly, the output from NOPA with a spectrum spanning 660 - 820 nm is compressed using a pair of prisms and then focused at the sample in a spot that has a effective beam spot size $2W_0$ (or beam diameter) around 133 μm and a energy of 15 nJ/pulse[4]. The non-polarizing beamsplitter is used to generate two pulse replicas, which are sent to two different retroreflectos, one of them is mounted on the computer-controlled translation state to introduce a controlled delay between the two pulses. These two beams are now identified as beams 1 and 2 (1+2) (stationary) and 3 and local oscillator (LO) (delayed). The beam 3+LO propagates through the rotating QWP modulating polarization as alternation of left- and right-circular polarization. Whereas, the beam 1+2 propagates to the RR1′ which is used as the pump beam, and is modulated by the Chp2. Subsequently, the beams 1+2 and

[2] the 1st and 3rd beam in Fig. 2.4 is unblocked

[3] It should be note that the temporal and spatial overlap between the four pulses and the size of the beam is crucial. The more focused the pulses into the sample, small probe volume of the sample will be excited thus, creating higher spatial resolution at that particular area of the sample. This lead to an advantage such as an isolated signal from source of noise such as scattering and spontaneous fluorescence emission. This is why boxcars geometry provide better clean and relatively high SNR compare to collinear phase-matching geometry [30–32]

[4] approximately equal to a fluence and number of photons about 1.078 mJ/mm^2 and 5.58×10^{10} photons, respectively

3+LO are directed onto a spherical mirror that focuses beams at 25 cm onto a transmission grating, working as a beamsplitter to generate four beams in total, as 1st and -1st order diffraction. The high-order diffraction is blocked by a spatial mask that only allows the first-order of diffraction to propagate through. The beam 1+2 and 3+LO must not overlap in the grating, as this can introduce the cross-phase modulation (XPM) between the two pairs of the beams[5] , which should be avoided.

Then, the four beams are reflected by M4 and SM2 ($f = 25$ cm) to reimage the spots in transmission grating on the sample. The combination of two SM and the transmission grating between them create a $2f$ imaging system. At the sample, one needs to overlap the four beams exactly in space to induce the third-order nonlinear processes in order to perform TA, TRCD, TGCD or 2DES. Experimentally, the population delay t_2 is achieved by using a computer controlled delay line (beams 3 and LO) (see Fig. 2.4). The generated signal is sent to the detection system which consists of the spectrometer (Acton SpectraPro 2300i, Princeton Instruments) and CCD camera (ELSE-s, Greateyes GmbH). The grating that is used in the spectrometer is 600 g/mm with the blaze angle centered at 750 nm and the readout CCD camera is 2353 Hz. As mentioned, the laser repetition rate was set to 11765 Hz (divider of 17 from 200 kHz).

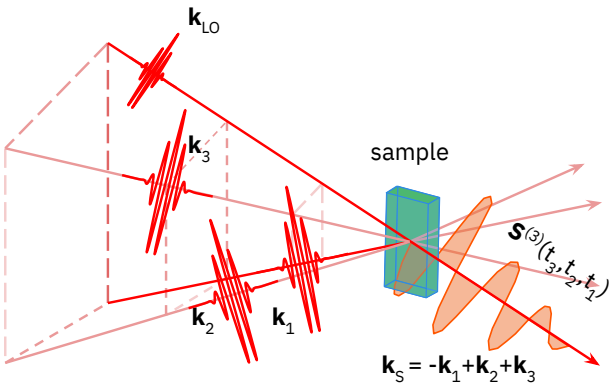

Figure 3.4: The third-order polarization response in spatial arrangement. The coherence time (between beam 1 and 2) t_1 and population time (between beam 2 and 3) t_2 can be set such that one can perform different time-resolved spectroscopy experiments. For example, when only the population time vary and only two beams are used, e.g. $\boldsymbol{k}_{LO}$ as probe and $\boldsymbol{k}_2$ or $\boldsymbol{k}_1$ as pump, pump-probe is obtained. Moreover, if both of the coherence and population time vary, two-dimensional spectroscopy can be obtained. If the coherence time $\boldsymbol{k}_2$ and $\boldsymbol{k}_1$ is set to 0 , heterodyne-detected transient grating can be obtained. The illustration is inspired by Ref. [33].

The quarter wave plate that is used for polarization modulation is the achromatic retarder consisting a quartz (640 μm) and MgF_2 (500 μm), all surfaces of the two crystals are anti-reflection coated with air gap (B.Halle Nachfl. GmbH) with a working spectral range of 600-1200 nm. It has group delay dispersion (GDD) of 37 fs^2 at 800 nm, thermal expansion coefficient of 0.25 nm/K, and angular coefficient of 0.8 nm/deg^2 for $\lambda/4$. Since, both materials are virtually free from absorption in the considered spectral range, one can

[5]XPM is a nonlinear process, involving isotropic medium or Kerr medium that has third order susceptibility $\chi^{(3)}$ [16]. This is occurs when two beams (ω_1 and ω_2) interact each other such that ω_1 is modulated by ω_2 and vice versa, inducing intensity-dependent refractive index, i.e. $\Delta n = \left(3\eta_o\chi^{(3)}/\epsilon_o n^2\right)(I_1 + 2I_2)$

assume that the losses are mainly due to the reflection at the four coated surfaces. Thus, each of the two has $R = 0.5(1 - T)$ or $R < 0.8\%$. These specification of the quarter wave plate ensure that there is little interference effect, and little refractive index modulation due to thermal expansion.

Another important component in the setup is the motor-driven chopper, indicated by Chp1 and either Chp2 or Chp3. When in use, the Chp1 has a frequency of about $f_1 = 114$ Hz, i.e. two times the reference frequency of 57 Hz and Chp3 has frequency of about $f_2 = 855$ Hz or 15 times of the reference frequency. Importantly, the rotating quarter wave plate also introduces a polarization modulation, to the laser pulses, generating another frequency f_{pol}. f_{pol} has a value about 114 Hz which is due to the fact that both LCP and RCP are induced twice in one full rotation (see Fig. 2.3). All of these modulations are crucial in the lock-in detection as will discussed in Sec. 3.3.2. The combination from most of the modulation frequencies occur in the Fourier transform spectrum of the sequence of signals measured with the CCD camera.

Before performing the test measurements, we also attempted to determine the sources of noise, for example coming from the vibration of the rotary state, and tried to suppress them. This is done by observing the Fourier spectrum of measured signals. By the observation of the peaks in the frequency spectrum, one can optimise the setup to find a way to suppress the peaks coming from vibrations and scattering. Practically, due to the mechanical vibration of the rotary stage mount when it rotates, this vibration generates forest of peaks at 708 - 826 Hz. These peaks are suppressed relatively well by utilizing an ethylene vinyl acetate (EVA) foam that has a thickness about 4 mm. This foam is inserted between the optical table and the bottom of the pedestal base and between the pedestal and the pedestal base. Furthermore, the other peaks around the signal frequencies are also due to the scattering from the sample, which in some conditions can be suppressed by moving the sample (see Sec. 3.4).

Table 3.1: The population scan parameters.

Population time (from)	Population time (to)	step
-1000	-1000	1
-40	200	20
300	2000	100
3000	20000	1000

For the TRCD measurements after setting up the lock-in filter frequency and phase, which is mostly done automatically by the program, the next step is to define the measurement settings. These include setting up the scan of the delay time from -552 to -488 fs with step 0.8 and population time as summarized in Tab. 3.1. This short scan of the delay time is introduced to perform a simple phase cycling[6] of the signal, aimed to suppress

[6]a method that the detected signal is a weighted summation of the signals of a series of experiment

scattering contribution from the pump beam.

3.3.2 Lock-in detection technique

Lock-in detection technique, also called phase-sensitive detection is an extremely powerful and versatile technique to deal with noisy signals. Our implementation of the lock-in filtering is based on a multiplication of a signal, modulated at a specific frequency, with a same frequency references in function and integration. For lock-in filtering to work, one needs to know exactly the signal modulation frequency and phase, which is achieved by synchronizing all the elements in the 2DES setup. It is often that in optical spectroscopy, the modulation is provided by introducing a motor-driven chopper to modulate the signal and provide the reference signal. In the experiments, presented here, all devices are synchronized using a pulse generator as a master clock: chopper, CCD camera read-out and a rotary stage. Measured signals are processed with the lock-in filtering algorithm in the computer to suppress the noise mainly from the scattering of the sample [14].

As an illustration, Fig. 3.5 shows lock-in Fourier spectrum where the pump and probe are modulated by the Chp3 and Chp1 (see Fig. 2.4), respectively. In the case of pump-probe experiments, the f_1 comes from the modulated probe beam that is modulated at 114 Hz[7], the f_2 comes from the scattering of the sample, and the pump-probe (PP) signal that can be at the sum $f_2 + f_1$ or difference $f_2 + f_1$ or both[8]. By performing necessary modulations of the laser pulses, and Fourier transforming the acquired data, one can specifically select which frequency peak is filtered out in the lock-in filter setting. The type of the filter function will determined the accuracy and the SNR ratio of the signal.

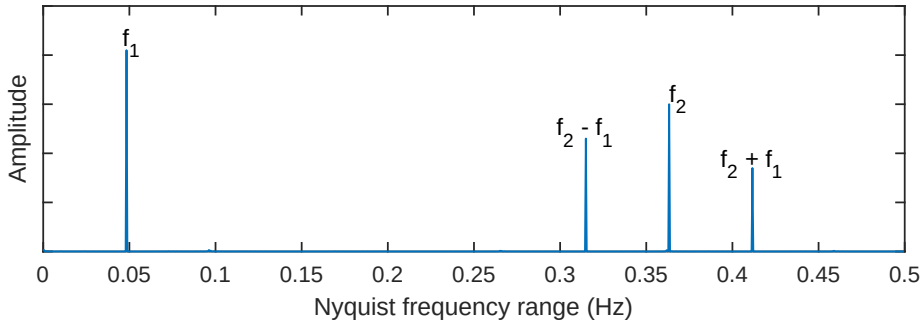

Figure 3.5: The ilustration of a lock-in spectrum. The frequencies on the x-axis are obtained by scaling the CCD readout rate (2353 Hz) with the relative frequency up to the Nyquist limit.

In this project, we use Welch window[9] which has parabolic function, tapering off, approximately, to zero at the edges of the time scan window. The advantages of Welch

repeated for different interpulses phases

[7] taking into account that the pump is always modulated at 855 Hz

[8] In our experiments, we take the average of the two

[9] $w(n) = 1 - \left(\frac{n-N/2}{N/2}\right)^2$ where n is the samplex index and N is the total number of samples, Ref. [34, 35]

window is three fold: 1) reduced spectral leakage for strong modulation frequencies that can infiltrate the signal from the sample, 2) preservation of the true characteristics of the signal and 3) improvement of the SNR ratio[10]. Therefore, using the Welch window for the data can potentially improve the isolation of the signal and the SNR ratio, necessary in TRCD due to extremely low signal level.

3.4 Sample handling

The sample that is used to test the TRCD setup is a chlorosomes containing *bacteriochlorophyll c* from green sulfur bacterium Chlorobaculum tepidum (*Cba. tepidum*). It was dissolved in the 50 mM Tris-HCl buffer (pH 8.0) and was diluted to absorbance about 0.3 in a 0.2 mm optical path cuvette at 739 nm. The sample was also moved in a raster scanning fashion[11] in the x-y plane by using a XY translational stage, with the attached home-made sample holder with a rectangular open area to let the laser illuminate the sample in the cuvette, this is shown in Fig. 3.6.

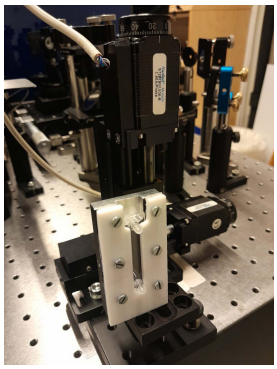

Figure 3.6: The home-made sample holder and the XY stage that is used when measurements were taken. Note that the vertical and horizontal motor drive the motion in vertical and horizontal direction, respectively.

By introducing this movement to the sample in the pump-probe measurement, the scattering noise, generated from the sample can be averaged out automatically without any processing algorithm. The movement of the sample seemingly did not help to increase the signal to noise ratio in the TRCD experiment, and even decreased it. However, we had to move the sample during the experiments as to avoid damaging the sample, because of the photobleaching[12].

[10] several studies in Ref. [36–40], mainly, in optical and laser spectroscopy in different applications, shows that Welch window, indeed has these advantages

[11] moving a sample in a systematic, grid-like pattern across two axes (X and Y). In our case both direction is move simultaneously

[12] a photoinduced damage of sample. Typically due to an oxidation of the sample that damage the sample permanently such that it can not emit any light

4 | Results and Discussion

In this chapter the experimental results are provided with the relevant discussion, which is connected to the information provided in in Chapter 2 and/or in Chapter 3.

4.1 Synchronization results

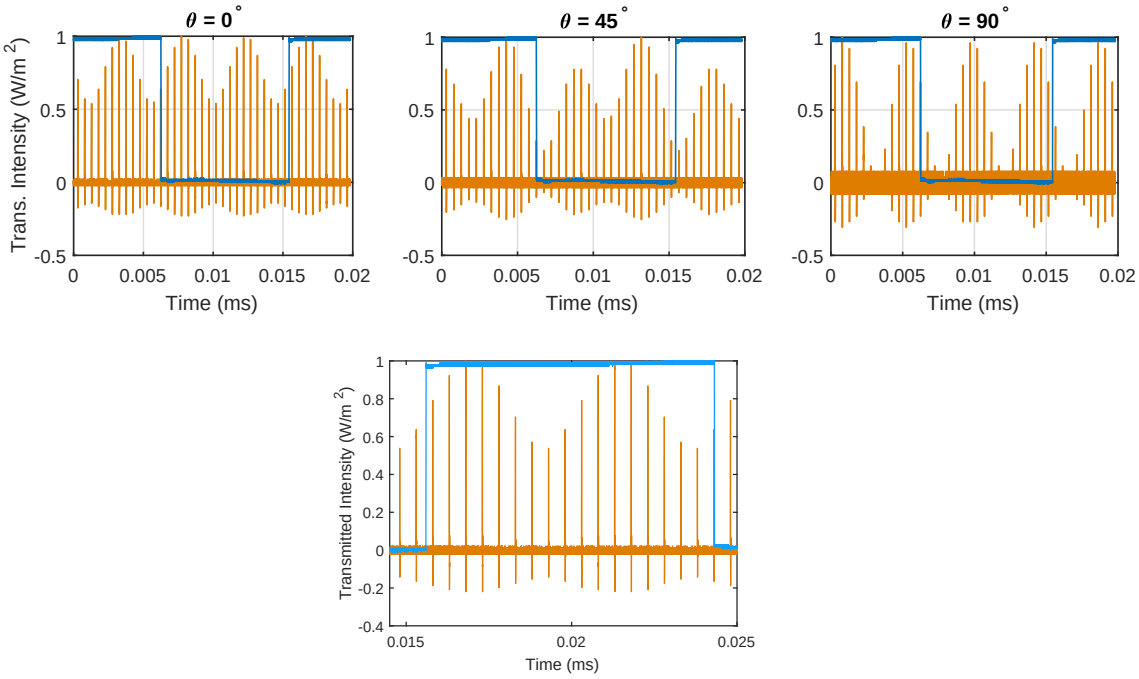

Figure 4.1: The synchronization results. Note that the θ angle in this figure denotes the orientation of the linear polarizer, in respect to the initial polarization of pulses. The blue solid line and orange spikes correspond to the trigger pulses (square pulses, coming from the pulse generator) and laser pulses which have polarization state changed after propagating through the rotating QWP, respectively. It should also noted that the transmitted intensity has been normalized to unity. The bottom figure shows a zoom in image when $\theta = 0°$

Synchronization of the chopper, rotary stage and CCD camera read-out Performing a synchronization measurement based on the setup shown in Fig. 3.3 with step[1] in Sec. 3.2.2 and guidance from Sec. 2.1.1, one could obtain a synchronization result in

[1] maintaining a stable frequency and phase among motor-driven rotary stage, motor-driven chopper and CCD read-out camera such that it stays and unshifted for longer time measurement

Fig. 4.1. Qualitatively, based on Fig. 4.1, it shows that the measured transmitted intensity[2] of the spike laser pulses, shows a similar behaviour compare to the simulation result in Fig. 2.3. For example, when the angle of linear polarizer is at $\theta = 90°$ (y-direction), the transmitted intensity maximum occurs four times during rotation period as expected (Fig. 2.3.). Moreover, there is a laser spike pulse that exactly matches with the falling edge of the blue square pulse, as seen in measurements with different linear polarizer angles. This match in timing of both signals, which always remains the same indicates that the sychronization works properly.

It is worth noting that the transmitted intensity, when the linear polarizer is at an angle of 45°, shows different maximum peak intensity for different circularly polarized light. The right circularly polarized (RCP) has, relatively, lower peaks transmitted intensity compare to the left circularly polarized (LCP). This might be due to some asymmetry of the efficiency of LCP and RCP laser pulse propagation through the setup, which will be investigated in the future studies.

Synchronization between the rotary stage and the chopper in the probe beam
Another important synchronization step is the synchronization between the Chp1 and the rotary stage. The idea is to apply the lock-in detection technique, which is implemented in the pump-probe measurement, to the TRCD measurement. This involves first setting the lock-in frequencies and phases for the signal filtering during pump-probe measurement, which is a standard procedure in the lab. The difference between the two experiments is that in pump-probe, the probe beam is modulated by the chopper (Chp1), and in TRCD, the same beam is polarization-modulated by the rotating QWP. Since the same lock-in parameters are used for extracting signals from both experiments, the modulation frequency and phase of both types of modulation have to be matched.

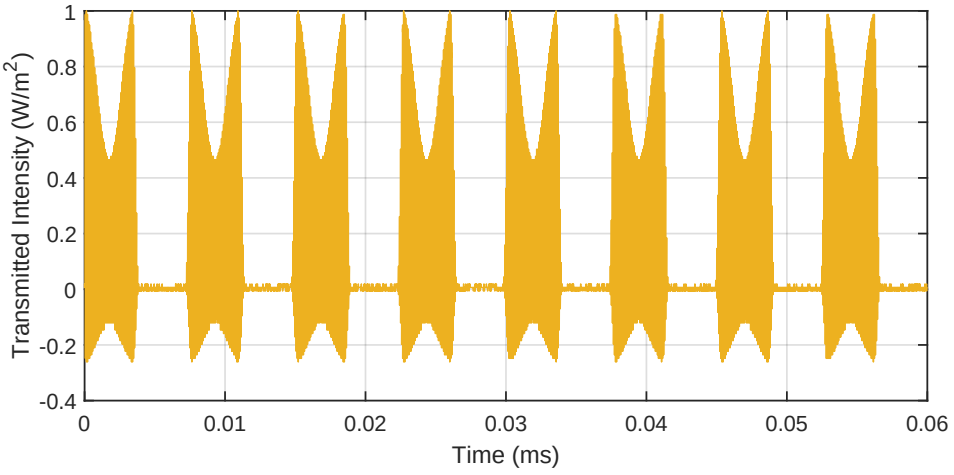

Figure 4.2: The phase matching between the probe modulation when using a chopper (PP experiment) and the rotating waveplate (TRCD experiment).

The motor-driven chopper and the rotary stage have the same modulation frequency

[2]the detail of voltage to the transmitted intensity conversion is provided in Appendix A.3

through the utilization of a pulse generator; however, not necessarily the same phase. However, the phase of probe modulation has to match also in order for the lock-in filtering in TRCD to work[3]. Practically, this can be achieved by changing the phase of the chopper such that the minima of the linearly filtered signal (indicating either RCP or LCP light) is matches the middle of the open chopper cycle[4]. Fig. 4.2 shows phase matching between the chopper and rotary stage modulation. After achieving this synchronization, the absorption difference between the left circular polarization (LCP) A_{LCP} and right circular polarization (RCP) A_{RCP} can be directly measured in our setup[5], using the lock-in filters set for the pump probe measurement.

4.2 Chlorosome absorption and circular dichroism

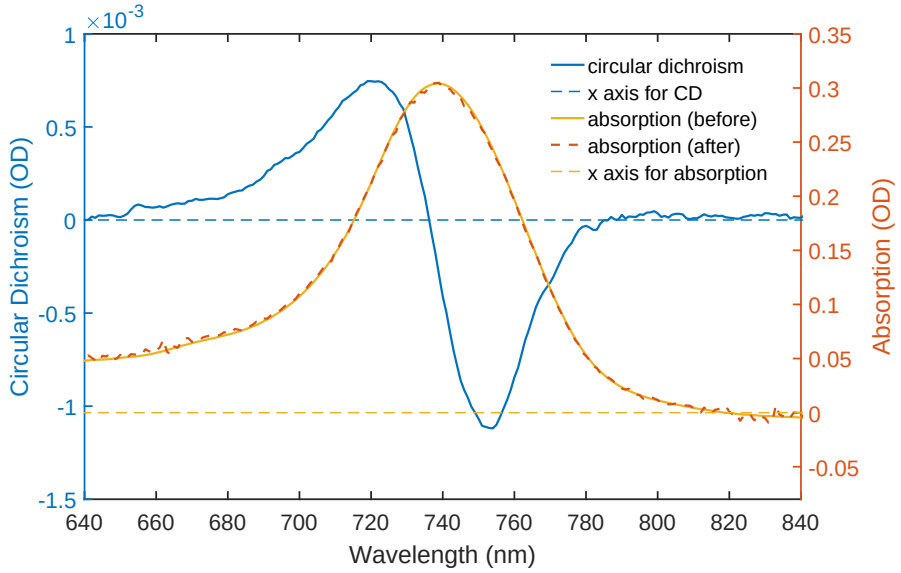

Figure 4.3: The absorption (orange solid line) and circular dichroism spectrum (blue solid line) of *Chl. tepidum* chlorosomes at room temperature. Note that both of the absorption and the CD spectrum are not normalized.

Performing absorption and ciruclar dichroism (CD) measurements are necessary before conducting the time-resolved absorption or TRCD experiments, as the this data will be

[3] further details is given in 3.3.2

[4] The setup is similar to the one that is used to evaluate the synchronization in Fig. 3.3

[5] This is done by first turning on Chp1 and setting the lock-in filter for the pump-probe (PP) measurement. After the lock-in filter setting is done for PP, Chp1 is turned off (see Fig. 2.4). When performing TRCD, the rotary stage is turned on while Chp1 is still off. The same lock-in setting for the PP measurement is used for the TRCD measurement. This is because PP is a nonlinear mixing process. The signals in the lock-in Fourier spectrum (Fig. 3.5) are also nonlinear and occur at the sum and difference frequencies. Since, we used the same setup, differing only in that PP uses amplitude modulation while TRCD uses polarization modulation. Thus, if the lock-in filter setting works for the PP signal, it will also work exactly the same for TRCD. Therefore, the CD signal of the absorption difference between A_{LCP} and A_{RCP} comes from this nonlinear mixing process that is occurs in the sum and difference frequencies

used as reference to the time-resolved spectrum both for pump-probe (TA) and TRCD. The steady-state absorption and CD spectrum is shown in Fig. 4.3. The absorption from chlorosomes has a broad absorption peak around 739 nm which is slightly shifted from previous measurements in Ref. [25], i.e. 745 nm. This peak corresponds to the excitonic Q_y band of the aggregated BChls *c*. This means that it has strong steady-state CD signal (see Sec. 2.4). It is also found that the full width half-maxium (FWHM) of the absorption band of 54 nm or 990 cm^{-1}. The reason of this peak shift is likely due to the fact that the sample that we use is more than ten years old and was stored in the fridge for that time. However, this result coincidentally is similar to the measurement that was presented in Ref. [28]. They found that the absorption peak is around 735-739 nm, yet they did not reported the FWHM of their absorption spectrum. Additionally, the absorption spectrum of the sample used in the TA, TRCD, and TGCD experiments was measured and is also provided, indicating that some BChl *c* in the chlorosome have been damaged during time-resolved measurements, even though with a relatively low percentage of degradation[6], i.e. 2%.

In addition to that, the CD spectrum of our sample is in good agreement with the result in Ref. [28], on the order of mdeg (millidegree)[7]. Furthermore, the CD spectrum is also of the type I, i.e. positive/negative [28]. Additionally, the peak and the valley of the CD spectrum is found to be around 722 nm and 754 nm, respectively. The physical phenomena behind this CD spectrum is the excitonic nature of transitions in this molecular aggregate (see Sec. 2.4). It is interesting to note that absorption peak and CD spectrum crossing zero line do not match perfectly. This is likely due to the fact that the CD spectrometer that is used in this study is not calibrated in the visible wavelength range, as it is mainly used in the UV range.

4.3 Measurements of time-resolved circular dichroism in chlorosomes

The most important results obtained in the test measurement are provided in this section. Firstly, the pulse characterization from the NOPA is discussed. Whereas the NOPA spectrum determines how much the steady-state absorption and circular dichroism is covered, the pulse duration dictates the temporal resolution needed to resolve the ultrafast dynamics of the photophysical phenomena. Secondly, the analysis of the signal-to-noise (SNR) ratio which is important to judge the capability of the developed direct TRCD setup that was build and the SNR comparison with other type of TRCD setups in relevant literature. Thirdly, the preliminary analysis of time-resolved absorption and circular dichroism intensity map, the comparison between the TA and TRCD spectra, and dynamics comparison between the TA and TRCD are shown. Lastly, a brief comparison analysis between TRCD

[6]It was obtained by subtracting the absorption before and after then took the absolute value of average of it

[7]The CD spectrum in the Fig. 4.3 is already converted from mdeg to OD by using relation $\Delta A \approx (\mathrm{CD} * (10^{-3}))/32.982$

and TGCD is also provided.

NOPA spectrum and the fit to the autocorrelation signal The NOPA spectrum and the compressed pulse duration were measured and are shown in Fig. 4.4.

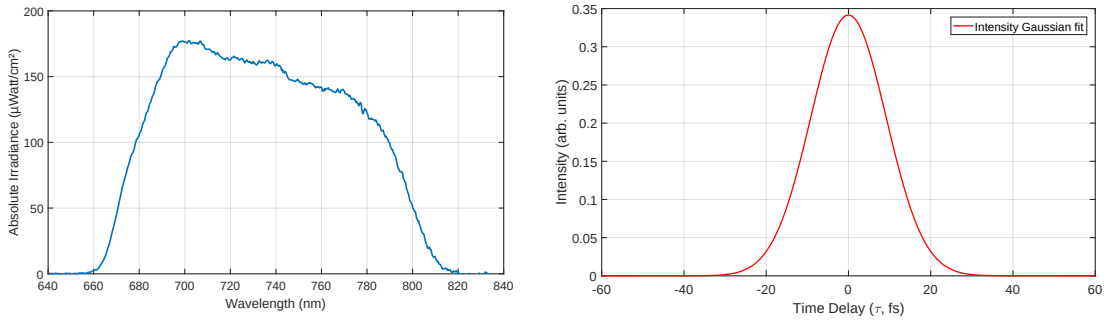

Figure 4.4: The pulse characterization of the NOPA output. The NOPA spectrum, covers wavelength in the range of 660 - 820 nm (left), the fit to the autocorrelation signal, obtained through second harmonic generation (SHG) between beam 2 and 4 (LO), that indicates pulse duration of around 16 fs (right).

The NOPA spectrum shows a nearly flat-top profile from single-amplification-stage NOPA. Wavelength range span from 660 to 820 nm, covering all of the absorption and most of CD spectra, shown in Fig. 4.3. This means that any photophysical process, triggered by the absorption of the chlorosomes can be observed. A brief description of phenomenon that leads to this spectrum was already discussed in Sec. 2.3.1. In time-resolved experiments, NOPA pulses were sent to the compressor made of a pair of prisms made of fused silica with an apex angle of 69.1° with the Brewster's angle of $\approx 55.6°$ to compress the pulse. The fit to the autocorrelation signal of the compressed pulses is shown on the right of Fig. 4.4. It is obtained by the generation of second harmonic (SHG) between beam 2 and 4 (LO) in Fig. 2.4 and it was found that the pulse duration was about 16 fs by performing an intensity Gaussian fitting to the autocorrelation signal. Since, the ultrafast dynamics of chlorosomes spanning from few hundred fs to ps, the pulse duration of 16 fs is sufficient to resolve all the ultrafast dynamics.

Signal-to-noise ratio analysis All above results are significantly important to yield reliable TRCD signal, particularly, the analysis of the SNR ratio as provided here. Following the idea from Ref. [41] by which they developed direct-TRCD that is less prone to polarization-artifacts compared to the ellipsometric-TRCD. The optical component that they used to generate very good quality of circularly polarized white light probe is a Pockels cell, i.e. electro-optic modulator, achieving an ellipticity lower than 4% and noise level of about 10^{-4} of absorbance unit (optical density) [41].

However, at that time, the slow read-out of dispersive detection using a CCD camera, required acquisition of trains of 40 consecutive probe pulses, alternating between left- and right-circular polarization, limiting the accuracy to 1 mOD [41]. Compared to that, our result shows that the noise level of our developed setup is on the order 2×10^{-5} as shown

in bottom of Fig 4.5 which is calculated from the standard deviation of the measured spectrum at -1000 fs[8]. This yield to SNR approximately about 12. This relatively high SNR ratio is calculated by averaging the TRCD spectrum at 200 fs and divided it with standard deviation of the TRCD spectrum at time delay -1000 fs.

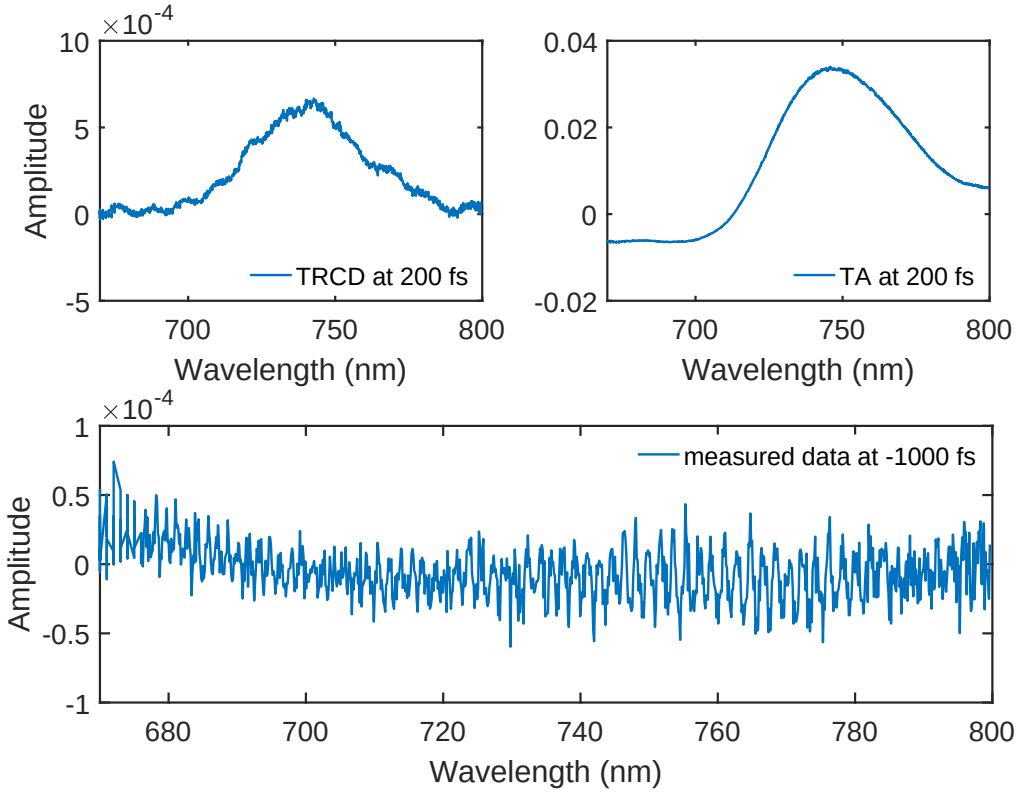

Figure 4.5: The TA and TRCD spectra at 200 fs in the units of differential absorbance for TA and TRCD. The top left shows the TRCD spectra while top right shows the TA spectra. The bottom figure shows the measurement where the probe beam comes about -1000 fs before the pump beam which means measuring the noise of the developed TRCD setup.

Moreover, the CD signal at a given wavelength λ and time delay Δt between vertically polarized pump excitation and circularly polarized probe is given by [41]

$$\mathrm{CD}(\lambda, \Delta t) = \Delta A_L(\lambda, \Delta t) - \Delta A_R(\lambda, \Delta t) \tag{4.1}$$

where A_L and A_R are the absorbance of the sample to left- and right-circularly polarized probe pulses (see 4.1). The setup, developed here, uses lock-in detection and thus measures this difference directly. Because of the use of fast read-out CCD camera, the acquisition time is much faster than the direct TRCD setup developed by Trifonov *et. al.*,. Our TRCD setup allows acquisition time approximately about two hours with parameters defined in Tab. 3.1, where each spectra is measured 90 times. The TRCD spectrum measured in this project is compared to the TA spectrum signal measured under the same conditions

[8]this means the probe comes earlier about -1000 fs before the pump beam

(Fig. 4.5). As expected, the TRCD spectrum is much weaker than TA, approximately 51 times[9]. Furthermore, the TRCD and TA spectra measured and the same delay time look completely different. These observations provide an indication that the developed direct TRCD setup is capable of measuring the TRCD signal.

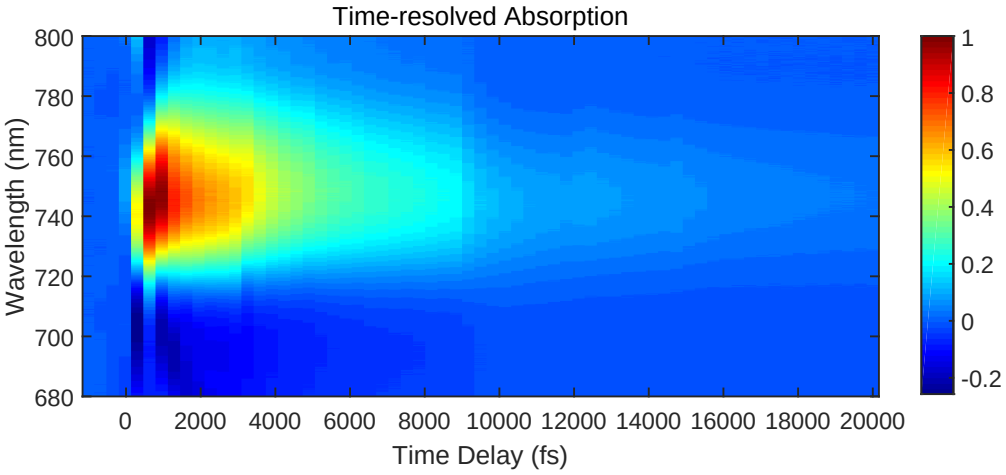

Figure 4.6: TA spectra of chlorosomes. Note that the signal is normalized to unity for clarity.

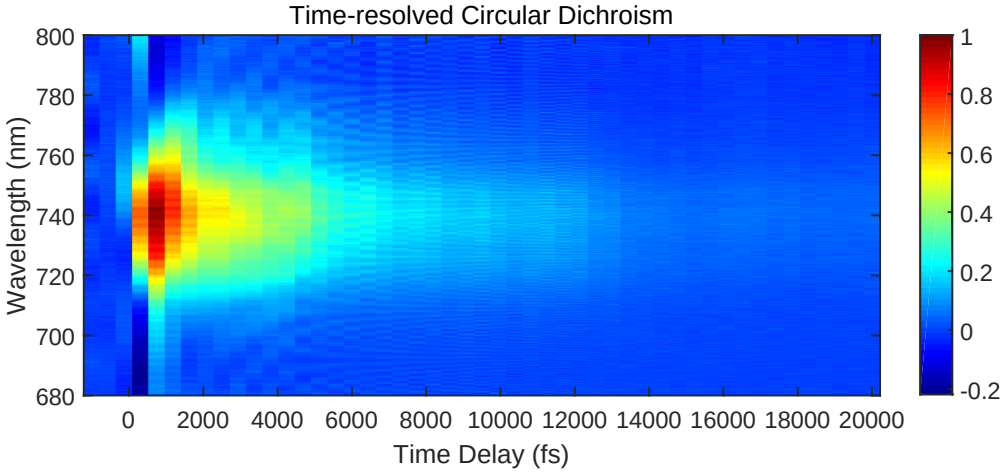

Figure 4.7: TRCD spectra map of chlorosomes.

TA and TRCD maps The estimated SNR ratio only shows that the developed direct TRCD is capable of measuring relatively small signals. It would be very useful to compare the measured TRCD spectra of chlorosomes to a known result. However, how the TRCD spectrum of chlorosomes should look like is unknown, as it has never been measured and there are no corresponding theoretical calculations. Potentially, the biggest complication

[9]By taking the peak maximum value of both TA and TRCD and take the ratio between them

in TRCD experiment could be that instead of measuring true TRCD spectra, the setup picks up attenuated TA spectra. Therefore, the only way, at the moment, to judge the capability of our direct TRCD is to compare it to the TA signal for the same sample and same conditions. This is shown in detail in Figs. 4.6 , 4.7 and 4.8.

Fig. 4.6 shows the TA dynamics of chlorosomes. Importantly, the TA and TRCD spectra, exhibit clear differences. Furthermore, the positive signal in the TA spectra are observed in the range of 720 - 785 nm, while the positive TRCD only spans 715 - 778 nm. Another clear difference is that in TA negative signal is observed in 680 - 715 nm range, indicating the excited state absorption, whereas in TRCD no such signal is detected. Lastly, the positive spectra in TA and TRCD also shows distinct dynamics. The former one depicts broad spectra while the later depicts narrower spectra.

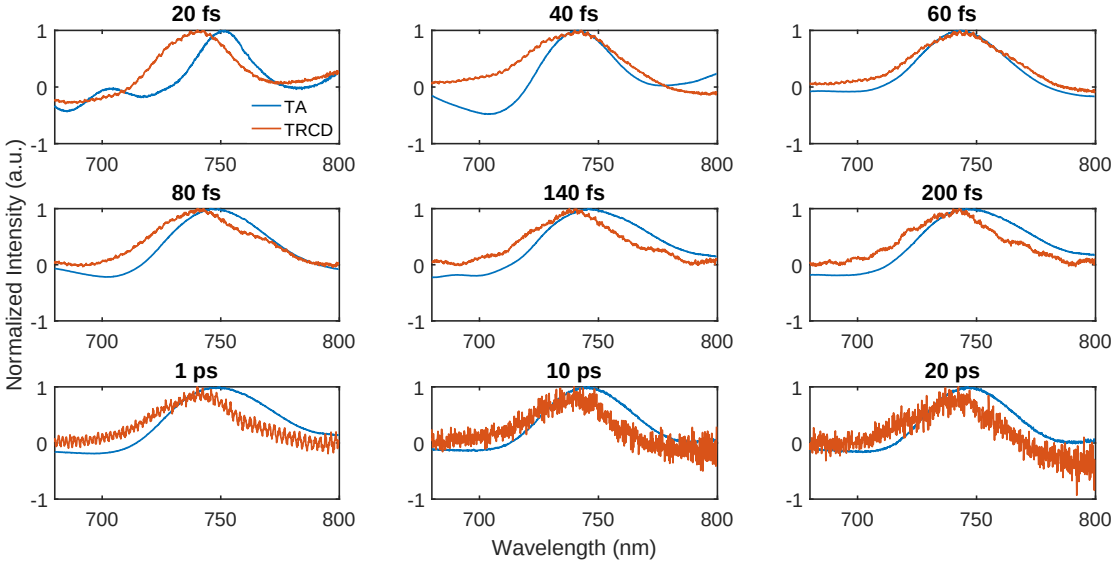

Figure 4.8: The comparison between TA and TRCD spectrum dynamics at certain time delays of interest.

Individual TA and TRCD spectra Further analysis of the TRCD spectrum is provided in this section. Fig. 4.8 depicts the time-resolved signal dynamics of chlorosomes at several time delays that correspond to several photophysical processes that were discussed in Sec. 2.4. According to Fig. 4.8, the TRCD signal shows different spectra for each time delay, indicating that it is a TRCD signal, and not a "leaked" TA signal. For example, at 20 fs, TA shows a complicated spectrum that is most likely due to the pulse overlap effects in this experiment, which distort true TA signal of chlorosomes. In contrast, TRCD spectrum at the same time delay shows a signal shape that remains similar for other time decays, indicating that this measurement is more immune to the pulse overlap artifacts. Additionally, another prominent difference between TA and TRCD is the positive signal for each of the time delays, i.e. in TRCD, it is found at around 736-743 nm and in TA - around 740-751 nm. This could be an indication that in TRCD, more dispersive type of

signals interfere, producing seeming shifted positive signal, but also lack of the negative signal in the 680 -715 nm range (see the discussion above). One of the expected source of this interference would be excited state absorption CD signal. However, the shape of this signal is unknown as it has never been measured or calculated.

At the later times, in contrast, the TRCD spectrum shows more noisy signal, due to the faster decay (Fig. 4.7). Starting from around 7 ps to 14 ps the scattering signal starts to substantially infiltrate the TRCD signal. Thus, the next step in evaluating the measured TRCD signal is to inspect the TRCD kinetics and compare them with the TA kinetics.

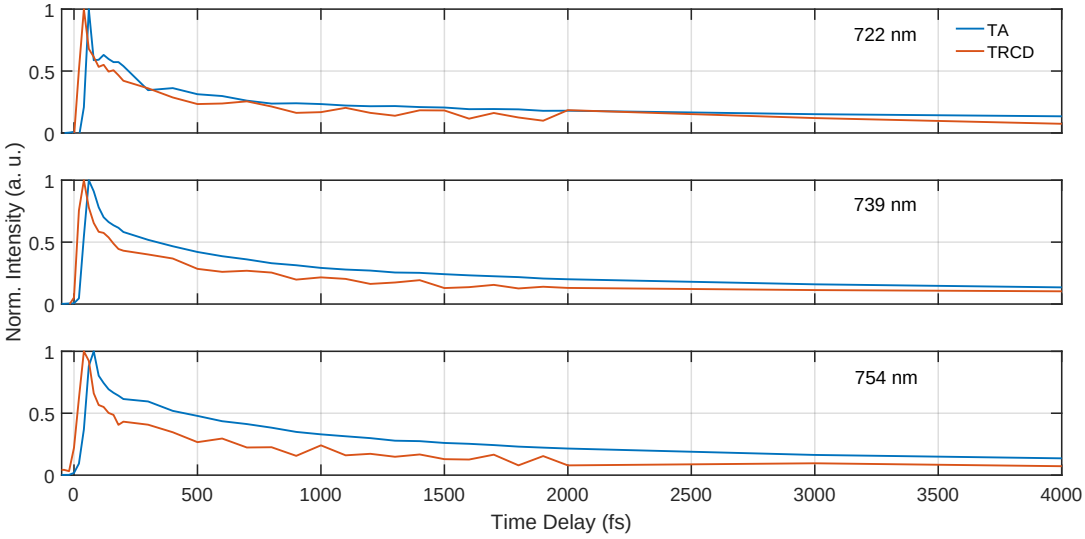

Figure 4.9: The chlorosome TA and TRCD kinetics comparison at selected probing wavelengths.

Kinetics observed in the TA and TRCD measurements The last approach to validate our TRCD test measurement, is to compare the TRCD kinetic traces with the kinetics of TA as depicted in Fig. 4.9. Firstly, the long-time dynamics in TA lasts up to around 50 ps while the TRCD decays at around 16 ps, indicating that TRCD pick up different ultrafast processes in the measurement. Moreover, as can be clearly seen, the differences of TRCD with respect to TA are persistent. First of all, the kinetics of TRCD starts earlier than TA at the chosen wavelengths of 722, 739 and 754 nm. The starting time delay point where the TRCD start to decay is always the same, 40 fs, while the TA signals start at 70 fs. This difference on the onset of the time-resolved signal in TRCD and TA measurements is most likely due to the additional delay in the TA measurement setup, even though the reason is not clear yet. Also, this delay difference observation has to be explored in future experiments. The most apparent difference, however, as mentioned above, is the difference in decay times of the signal. Whereas the TRCD signals decays with the similar time as TA signal at 722nm, it is notably faster at 739 nm, with further increasing difference at 754 nm. The origin of these differences are unknown, and if confirmed will require theoretical modeling. At this point, one could only speculate that

at different wavelength, the TRCD signal decays faster, because energy is transferred from higher- to lower-energy excitonic states in the chlorosome, assuming that lower excitonic states have lower chiral signal. This can be looked at as a chirality transfer.

A demonstration of heterodyne-detected transient grating circular dichroism
The intention of this section is to provide a demonstration that the developed TRCD setup can be extended to perform TGCD measurement[10] as discussed in detail in Sec. 2.3.3. The result from TGCD is analyzed using an in house 2DES analysis program and it is shown in Fig. 4.10. In principle, TA signal and TGCD signal carry the same information, even though they are measured in substantially different ways. Because of the difference in measurements, they can have different levels of noise which is useful to compare. In Fig. 4.10 the TGCD spectrum at 60 fs is compared to the TRCD spectrum at the same delay time. Both spectra are similar and feature similar noise level. Importantly, this demonstrates that even CD 2DES experiments are feasible, as 2DES experiments are done in exactly the same way as TRCD, but in addition of population time, coherence time between pulses 1 and 2 are also scanned. CD 2DES experiments are the long-term goal in the laboratory and will provide even more information on chiral signals of different materials.

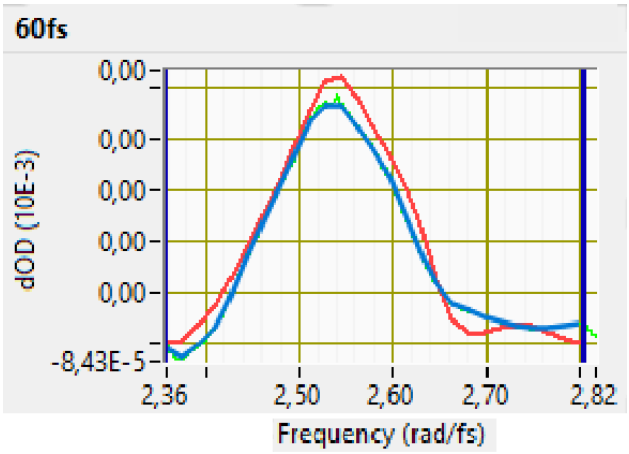

Figure 4.10: The comparison of TGCD and TRCD spectra at 60 fs. The blue solid line shows the TRCD while the red solid line is the TGCD data.

[10]However, since the measurement setting is different, i.e. the pulse energy is 10 nJ, one could not really compare between TGCD with the TRCD. That is why the aim of this discussion is to demonstrated that the TGCD, can be achieved, regardless that there are technical issues.

5 | Conclusion and Outlook

The main goals of this project are as follows, to develop an novel TRCD spectroscopy setup by utilizing a mechanically rotating quarter-wave plate in the existing two-dimensional electronic spectroscopy setup, achieve a relatively high signal-to-noise ratio with minimal polarization artifacts, and to perform a test measurements.

The main results of this work include development of direct TRCD setup with the capability to measure the TRCD signals with relatively high SNR. To achieve this, the setup utilizes double-modulation lock-in detection, which has proven to be extremely efficient in extracting weak signals, which are drowned in noise. The test TRCD measurements of a molecular aggregate chlorosome feature persistent differences between the TA and TRCD spectra, indicating that setup is capable of discerning real TRCD signals. It was also demonstrated that setup can reliable measure heterodyne-detected transient grating CD signals.

The continuation of this project involves measuring an achiral sample, lacking any CD signal, to verify the TRCD setup accuracy and determine the lowest measurable signal level. Next experiment that will be developed and characterized is the two-dimensional electronic spectroscopy circular dichroism (2DCD), which has been a long-sought after technique, with a potential to reveal intricate mechanisms and complex ultrafast dynamics in materials featuring chiral transitions, such as low dimensional semiconductors.

Contribution statement and reflection on my work

During my time working on this thesis project, I have performed several tasks. First, I created a home-made jig to correctly align six holes on the quarter-wave plate holder to the rotation stage as shown in Fig. 3.2, and designed the template myself. I designed and built the rotary stage cooling system myself. I also helped build the synchronization setup shown in Fig. 3.3, particularly assembling the rotation stage with the controller and connecting the controller to the pulse generator.

Furthermore, I conducted synchronization procedures with my supervisor and performed several measurements to validate excellent synchronization between all instruments. Moreover, I independently conducted steady-state absorption and CD measurements and analyzed the data. An important part of my work involved preparatory pump-probe/2DES measurement routines that are strongly related to my education in photonics. This included aligning beams in the NOPA instrument, and checking the overlap of all beams at the sam-

ple position in space and time using beam profiler, and second harmonic autocorrelation setup, respectively. I was involved in determining time zero and assisted my supervisor in beam alignment when the quarter-wave plate, along with its rotation stage and mount, were introduced into the 2DES setup.

I also learned how to optimize pulse compression using a pair of prisms, how to adjust the angle of the BBO crystals, and the z-position. Additionally, I learned and assisted in the spectrometer calibration, and the lock-in setup. Furthermore, I learned and performed all the sample handling in the chemistry laboratory.

Lastly, I learned how to perform the full ultrafast spectroscopy routine, from setting up the NOPA with its optical tricks, including cleaning of optical elements and beam alignment, to carrying out measurements. The measurements of TA and TRCD was mostly conducted with the help from my supervisor, while I mostly handled data analysis. Another important learning outcome was obtaining practical knowledge of all the necessary simulations for the validation of synchronization, a topic I found intriguing from the start, as it is not widely discussed in lectures. Finally, I must say, I have learned many valuable things in this thesis project that will greatly benefit my future career as a university lecturer in Indonesia, where I also plan to develop an ultrafast spectroscopy setup.

References

1. Changenet, P. & Hache, F. Recent advances in the development of ultrafast electronic circular dichroism for probing the conformational dynamics of biomolecules in solution. *The European Physical Journal Special Topics,* 1–13 (2022).
2. Mitchell, Z. A. *FIRST PRINCIPLES MODELING AND TIME-RESOLVED CIRCULAR DICHROISM SPECTROSCOPY OF THE FENNA-MATTHEWS-OLSON COMPLEX* PhD thesis (Purdue University Graduate School, 2022).
3. Kliger, D. & Lewis, J. Recent advances in time resolved circular dichroism spectroscopy. *Reviews of chemical intermediates* **8,** 367–398 (1987).
4. Changenet, P. & Hache, F. Artifact-free balanced detection for the measurement of circular dichroism with a sub-picosecond time resolution. *Optics Express* **31,** 21296–21310 (2023).
5. Oppermann, M. *et al.* Ultrafast broadband circular dichroism in the deep ultraviolet. *Optica* **6,** 56–60 (2019).
6. Bonmarin, M. & Helbing, J. Polarization control of ultrashort mid-IR laser pulses for transient vibrational circular dichroism measurements. *Chirality: the pharmacological, biological, and chemical consequences of molecular asymmetry* **21,** E298–E306 (2009).
7. Hache, F. & Changenet, P. Multiscale conformational dynamics probed by time-resolved circular dichroism from seconds to picoseconds. *Chirality* **33,** 747–757 (2021).
8. Dartigalongue, T. & Hache, F. Precise alignment of a longitudinal Pockels cell for time-resolved circular dichroism experiments. *JOSA B* **20,** 1780–1787 (2003).
9. Ghosh, S. *et al.* Broadband optical activity spectroscopy with interferometric Fourier-transform balanced detection. *ACS photonics* **8,** 2234–2242 (2021).
10. Ress, L. *et al.* Time-Resolved Circular Dichroism of Excitonic Systems: Theory and Experiment on an Exemplary Squaraine Polymer. *Chemical Science* (2023).
11. Stadnytskyi, V., Orf, G. S., Blankenship, R. E. & Savikhin, S. Near shot-noise limited time-resolved circular dichroism pump-probe spectrometer. *Review of Scientific Instruments* **89** (2018).
12. Morgenroth, M., Scholz, M., Lenzer, T. & Oum, K. Ultrafast UV–vis transient absorption and circular dichroism spectroscopy of a polyfluorene copolymer showing large chiral induction. *The Journal of Physical Chemistry C* **124,** 10192–10200 (2020).

13. Morgenroth, M. *et al.* Mapping the broadband circular dichroism of copolymer films with supramolecular chirality in time and space. *Nature communications* **13,** 210 (2022).

14. Augulis, R. & Zigmantas, D. Two-dimensional electronic spectroscopy with double modulation lock-in detection: enhancement of sensitivity and noise resistance. *Optics express* **19,** 13126–13133 (2011).

15. Paleček, D. & Zigmantas, D. Double-crossed polarization transient grating for distinction and characterization of coherences. *Optics Express* **26,** 32900–32907 (2018).

16. Saleh, B. & Teich, M. *Fundamentals of Photonics* ISBN: 9781118770092 (Wiley, 2019).

17. Lininger, A. *et al.* Chirality in light–matter interaction. *Advanced Materials* **35,** 2107325 (2023).

18. Schellman, J. A. Circular dichroism and optical rotation. *Chemical reviews* **75,** 323–331 (1975).

19. Parson, W. W. *Modern optical spectroscopy* (Springer, 2007).

20. Mukamel, S. Principles of nonlinear optical spectroscopy. *(No Title).*

21. Weiner, A. M. *Ultrafast optics* (John Wiley & Sons, 2011).

22. Foot, C. J. *Atomic physics* (OUP Oxford, 2004).

23. Xu, Q.-H., Ma, Y.-Z. & Fleming, G. R. Heterodyne detected transient grating spectroscopy in resonant and non-resonant systems using a simplified diffractive optics method. *Chemical physics letters* **338,** 254–262 (2001).

24. Zigmantas, D., Poli´vka, T., Persson, P. & Sundström, V. Ultrafast laser spectroscopy uncovers mechanisms of light energy conversion in photosynthesis and sustainable energy materials. *Chemical Physics Reviews* **3** (2022).

25. Dostal, J. *et al.* Two-dimensional electronic spectroscopy reveals ultrafast energy diffusion in chlorosomes. *Journal of the American Chemical Society* **134,** 11611–11617 (2012).

26. Fujita, T., Brookes, J. C., Saikin, S. K. & Aspuru-Guzik, A. Memory-assisted exciton diffusion in the chlorosome light-harvesting antenna of green sulfur bacteria. *The Journal of Physical Chemistry Letters* **3,** 2357–2361 (2012).

27. Márquez, A. S., Chen, L., Sun, K. & Zhao, Y. Probing ultrafast excitation energy transfer of the chlorosome with exciton–phonon variational dynamics. *Physical Chemistry Chemical Physics* **18,** 20298–20311 (2016).

28. Furumaki, S. *et al.* Circular dichroism measured on single chlorosomal light-harvesting complexes of green photosynthetic bacteria. *The Journal of Physical Chemistry Letters* **3,** 3545–3549 (2012).

29. Martiskainen, J., Linnanto, J., Aumanen, V., Myllyperkiö, P. & Korppi-Tommola, J. Excitation energy transfer in isolated chlorosomes from Chlorobaculum tepidum and Prosthecochloris aestuarii. *Photochemistry and photobiology* **88,** 675–683 (2012).

30. Eckbreth, A. C. BOXCARS: Crossed-beam phase-matched CARS generation in gases. *Applied Physics Letters* **32,** 421–423 (1978).

31. Prior, Y. Three-dimensional phase matching in four-wave mixing. *Applied Optics* **19,** 1741_1–1743 (1980).

32. Romanov, D., Filin, A., Compton, R. & Levis, R. Phase matching in femtosecond BOXCARS. *Optics letters* **32,** 3161–3163 (2007).

33. Bukarte, E. Big Lessons from Small Bacteria: Following Photo-driven Processes in Photosynthetic Systems with Multidimensional Spectroscopy (2023).

34. Heinzel, G., Rüdiger, A. & Schilling, R. Spectrum and spectral density estimation by the Discrete Fourier transform (DFT), including a comprehensive list of window functions and some new at-top windows (2002).

35. Jwo, D.-J., Chang, W.-Y. & Wu, I.-H. Windowing techniques, the welch method for improvement of power spectrum estimation. *Comput. Mater. Contin* **67,** 3983–4003 (2021).

36. Bruchhausen, A. *et al.* Investigation of coherent acoustic phonons in terahertz quantum cascade laser structures using femtosecond pump-probe spectroscopy. *Journal of Applied Physics* **112** (2012).

37. Borns, D., Hovde, D., Chen, S. & Sivler, J. *Early fire sensing using near IR diode laser spectroscopy* in *Proc. SPIE* **4817** (2002), 73–81.

38. Parfentyeva, V. *et al.* Fast time-domain diffuse correlation spectroscopy with superconducting nanowire single-photon detector: system validation and in vivo results. *Scientific Reports* **13,** 11982 (2023).

39. Nemes, L., Brown, E. E., Yang, C. S.-C. & Hommerich, U. Mid infrared emission spectroscopy of carbon plasma. *Spectrochimica Acta Part A: Molecular and Biomolecular Spectroscopy* **170,** 145–149 (2017).

40. Sitnikov, D., Romashevskiy, S., Pronkin, A. & Ilina, I. *Open-path gas detection using terahertz time-domain spectroscopy* in *Journal of Physics: Conference Series* **1147** (2019), 012061.

41. Trifonov, A., Buchvarov, I., Lohr, A., Würthner, F. & Fiebig, T. Broadband femtosecond circular dichroism spectrometer with white-light polarization control. *Review of Scientific Instruments* **81** (2010).

42. *Large Area Photoreceivers Models 2031, 2032, 2033 and 2034* Document number 203107 Rev. C. New Focus, Inc. (2001).

43. *ACSPL+ Commands & Variables Reference Guide* Rev. 3.10. ACS MotionControl Ltd (2021).

A | Matlab scripts

A.1 Rotating QWP polarization ellipse

```
% Set the initial parameters
Jvertilinear = [0 ; 1]; % Jones vector for vertical linear polarization
Im = 1j; % Imaginary unit
theta_deg = linspace(0, 180, 9); % Define the rotation angles (for plotting
    the polarization ellipse)
theta = deg2rad(theta_deg); % Convert angles to radians
qwp = [1 0 ; 0 -Im]; % Jones matrix for a QWP

% Define rotation matrix
rot = @(theta) [cos(theta) -sin(theta); sin(theta) cos(theta)];

% Rotate the QWP and determine the resultant Jones matrix
Jafterqwp = zeros(2, length(theta));
for i = 1:length(theta)
    %rotated_qwp = rot(-theta(i))*qwp_rotated*rot(theta(i));
    rotated_qwp = rot(theta(i))*qwp*rot(-theta(i));
    Jafterqwp(:,i) = rotated_qwp*Jvertilinear;
end

% Extract magnitude and phase from Jones vectors
magx = abs(Jafterqwp(1,:));
phasex = angle(Jafterqwp(1,:));
magy = abs(Jafterqwp(2,:));
phasey = angle(Jafterqwp(2,:));

% Calculate the phase difference delta for each theta
delta = phasey - phasex;

% Calculate the components Ex and Ey for each theta and t
t = linspace(0, 2*pi, 1000);
Ex = zeros(length(t), length(theta));
Ey = zeros(length(t), length(theta));
for i = 1:length(theta)
    Ex(:,i) = magx(i)*cos(t);
    Ey(:,i) = magy(i)*(cos(delta(i))*cos(t) - sin(delta(i))*sin(t));
end

```

```
% Plot the polarization ellipses directly from Ex and Ey
figure;

for i = 1:length(theta)
    subplot(3, 3, i);  % Adjust the grid size as needed

    % Plot the ellipse
    plot(Ex(:,i), Ey(:,i), 'b', 'LineWidth', 1.0);
    grid on
    axis equal;
    xlim([-1.0 1.0]);
    ylim([-1.0 1.0]);

    title(['\theta = ' num2str(theta_deg(i)) 'deg']);

    % Add annotations for the polarization state
    if abs(delta(i) - pi/2) < 0.1 && abs(magx(i) - magy(i)) < 0.1
        text(0.6, 0.9, 'RC');
    elseif abs(delta(i) + pi/2) < 0.1 && abs(magx(i) - magy(i)) < 0.1
        text(0.6, 0.9, 'LC');
    elseif delta(i) > 0 && abs(magx(i)) > 0.1
        text(0.6, 0.9, 'RE');
    elseif delta(i) < 0 && abs(magx(i)) > 0.1
        text(0.6, 0.9, 'LE');
    elseif abs(magx(i)) < 0.1
        text(0.6, 0.9, 'V');
    end
end
%}
```

Listing A.1: The matlab script for simulating the polarization ellipse of laser pulses after propagate through rotating QWP

A.2 Transmitted Intensity simulation

```

% Initial Jones vector for the polarization state of light/laser beam
VP = [0; 1];
lp = [1 0; 0 0];
retro = [-1 0; 0 -1];
M1 = [1 0; 0 1];
M2 = [1 0; 0 -1]; %M2=M3=M4
SM1 = [-1 0; 0 -1];
alphadeg = 0;
alpha = deg2rad(alphadeg);
rot = [cos(alpha) -sin(alpha); sin(alpha) cos(alpha)];
rotSM = rot*SM1;

% Define analyzer's Jones matrix
phi = 0; % Angle of analyzer
```

```
phirad = deg2rad(phi);
rotaposLP = [cos(phirad) -sin(phirad); sin(phirad) cos(phirad)];
rotanegLP = [cos(phirad) -sin(-phirad); sin(-phirad) cos(phirad)];
LP = rotaposLP*lp*rotanegLP;

times = linspace(0, 0.06, 6000000); %time in milisecond, to mimic actual number of data from oscilloscope

% Define quarter-wave plate's Jones matrix
Q = @(theta) [cosd(theta)^2 - 1i*sind(theta)^2, -(1 + 1i)*cosd(theta)*sind(theta);
              -(1 + 1i)*cosd(theta)*sind(theta), sind(theta)^2 - 1i*cosd(theta)^2];

% Calculate the transmitted intensity for each angle of the quarter-wave plate
angles_simulated = linspace(0, 1080, 6000000);
intensity_simulated = zeros(1, length(angles_simulated));

A = retro*VP;
B = M1*A;

for idx = 1:length(angles_simulated)
    theta = angles_simulated(idx);
    C = Q(theta)*B;
    D = M2*C;
    E = M2*D;
    F = (SM1*E);
    G = M2*F;
    H = (rotSM*G);
    J = LP*H;
    intensity_simulated(idx) = (abs(conj(J')*J));
end

intensitysimulated0degnooffsetdeg=intensity_simulated(1:6000000);

figure;
plot(times, intensitysimulated0degnooffsetdeg, 'LineWidth', 1); % simulated data
hold on;
plot(times, normintensity0deg, 'LineWidth', 1); % the experimental data
plot(times, normtrigger, 'LineWidth', 1); % the trigger pulse from oscilloscope
xlabel('Time (ms)');
ylabel('Transmitted Intensity');
legend('Simulated', 'Measured', 'Trigger pulse');
grid on;
```

Listing A.2: The matlab script for simulating the transmitted intensity

A.3 Voltage to Intensity conversion

The main output data from the photodiode that is connected to the oscilloscope is output voltage. As provided in the manual of large-area photodetector model 2023 [42], the conversion from output voltage to intensity is summarized through a matlab code below.

```
%oscilloscope data processing
%to convert output voltage to intensity from photodiode
R = 0.35; % A/W, the UV-enhanced silicon photodiode responsivity from
    Newport Series 2032 large area pd
G =1e5; %V/A, the medium amplifier gain
power=V180deg(:,3)./(R*G); %the output voltage data goes here
d = 5.8e-3; %diamter of the photodiode in meter
area = pi*(d/2)^2; %area of the photodiode
transmittedintensity = power./area; %
```

It should be note that all the processed data used photodiode responsivity of 0.35 due to the sake for simplicity data processing. Since, the amount of data generated from oscilloscope is 10^6, involving the actual responsivity value for each wavelength would be computationally demanding and time-consuming.

B | Thermal management

B.1 Temperature and electrical output power measurement

Temperature measurement In order to measure the temperature of the rotation stage when it rotates rapidly, one could use the digital thermometer with a metal probe tip that is attached to the rotation stage directly. The measurement was taken in the cylindrical side of the rotation stage with the help of optical mount as shown in Fig. B.1 below.

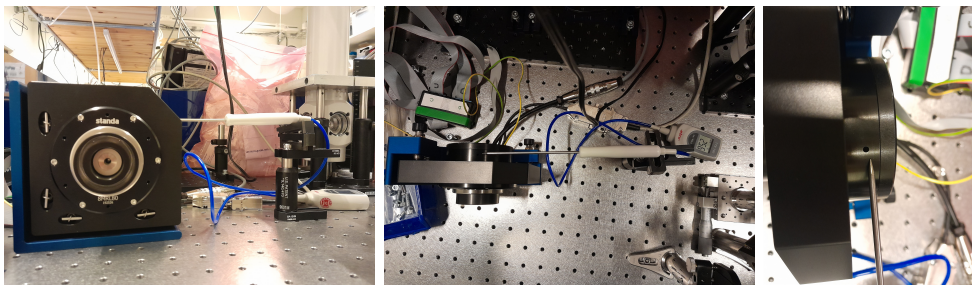

Figure B.1: The temperature measurement setup. The setup from front (left), top (middle) and the zoom in view from the top (right). It worth noting that the mount of the rotation stage, indeed, was not attached properly with a clamp, this is because one could also check at what rotation speed in Hz does the mount started to vibrate.

Before the temperature measurement, the tip of the digital thermometer was keep attached to the cylindrical side of the rotation stage up to, for approximately, 10 minutes to stabilize the surrounding temperature and the tip temperature to have the similar starting temperature. The temperature of the rotation stage was measured within in two minutes for each rotation speed, from 10 to 45 Hz, with rest time about one minute. The total temperature measurement was around 20 minutes, including the rest time between temperature transition measurements. The result from this measurement is shown in Fig. B.2. According to Fig. B.2, it is obvious that as the rotation speed of the jig in the rotation stage increases, the temperature of the rotation stage also increases, denoting linear trend.

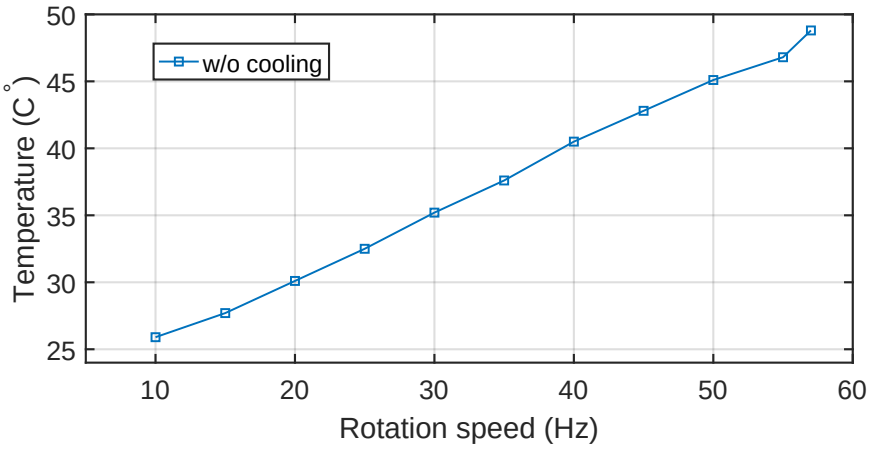

Figure B.2: The temperature measurement result from Fig. B.1. It should keep worth note that in this thesis 1 Hz=360 deg/s.

Electrical output power measurement To support this measurement, the electrical output power, that is used by the rotation stage when it rotates, was also done by using stander socket power meter. This socket power meter is connected parallelly to the connection where the power cable of the controller of the rotation stage is attached. It was found that the output power of the rotation stage was around 100 Watt and 15 Watt when its rotates and off, respectively, meaning that the rotation stage used about 85 Watt. By assuming that the efficient of the rotation stage controller was 85%, hence the approximated power that is used by the rotation stage is 72.25 Watt. By considering thermodynamics effect, one can use relation below to find the appropriate flow rate to cooled down the rotation stage that used power of 72.25 Watt. Namely,

$$Q = mc\Delta T \tag{B.1}$$

where Q is the heat in Joule/s (Watt), m is mass, c is the specific heat capacity for water, and ΔT is the temperature change. By re-writing Eq. B.1, one could obtain that the flow rate is approximately 17.20 ml/s. Hence, the appropriate water pump that is need to flow water inside a tube in the water cooling system should provide at least 20 ml/s flow rate.

B.2 Water cooling system

Based on rough estimation from Appendix B.1, one could determine the suitable water pump to cool down the rotation stage. Fortunately, the standard water pump flow rate for processor cooling in CPU is usually larger than 20 ml/s, basically one could use any water pump for processor cooling, yet in this thesis it was decided to use a DC 12 Volt water pump with a flow rate of 20 L/min from Koolance. The schematic of the water cooling system is shown in Fig. B.3 below.

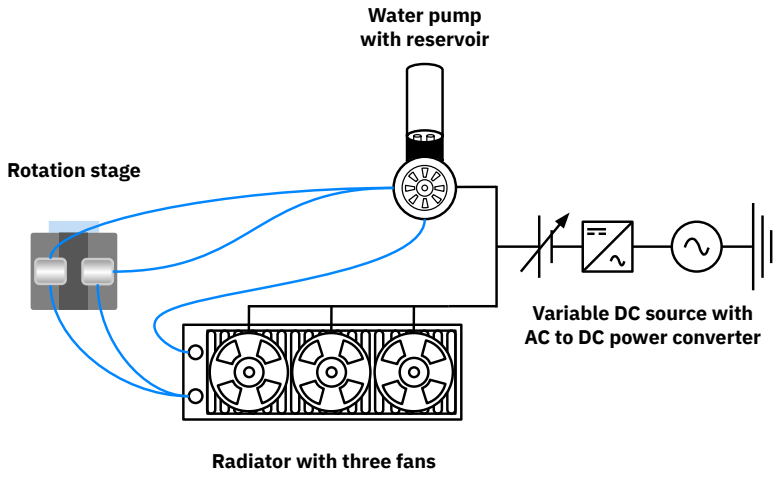

Figure B.3: The schematic arrangement of the water cooling system used in this thesis. Note that the blue curved line represent the PVC tube (G 1/4", i.e. 6 mm inner diameter and 10 mm external diameter) and the black line connection represent the wiring cables. Moreover, the cold plat that is attached to the rotation stage, basically, can be attach at possible area both in the rotation stage itself and the mount which is depend on the specific 2DES setup arrangement.

Additionally, the important component that is the radiator or heat exchanger. For efficient and optimal heat exchange, the radiator that is used in this case has a 30 fins/inch (FPI) with a thickness about 54 mm and compatible for three fans (3×120 mm). Another crucial part, that should be noted, is the placement of the cold plate whether to the rotation stage or the rotation stage mount or both of them. Basically, one could place and attach the cold plate to any possible area that can provide efficient heat exchanger. However, this placement will be vary depend on the complexity of the 2DES setup that is available. In this thesis, the placement of the cold plate is shown in Fig. B.4 below and the measured temperature as function of rotation speed also provided below.

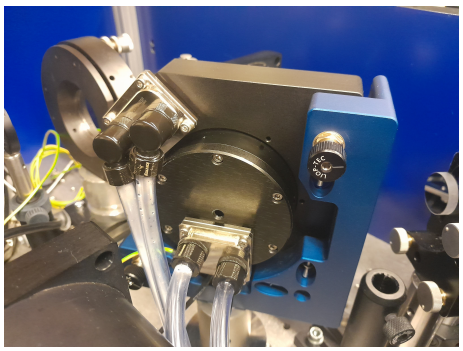

Figure B.4: The placement of the cold plates both to the rotation stage mount and the back side of it. In this thesis, thermally conductive adhesive WLK 5 from Fischer Elektronik is used to attach the cold plates with the help of clamps. It worth noting that the curing time at 20°C is approximately 20 hours.

When the water cooling system is installed, it was obvious that from Fig. B.5 the temperature is lower than before, indicating that the water cooling system works. However, due to the large difference in height between the cold plate and the water pump and water reservoir, the rate of the heat exchange was inefficient (the 1st test with cooling system or orange line). Nevertheless, the temperature shown by the green lime line has a lower temperature compare to the 1st test. This is due to relatively small height difference between the cold plate and the water pump and reservoir. In fact, for optimal and efficient heat exchange, one should put the water pump

and reservoir relatively near the cold plate to significantly enhanced the flow rate, thus enhancing the rate of the heat exchange.

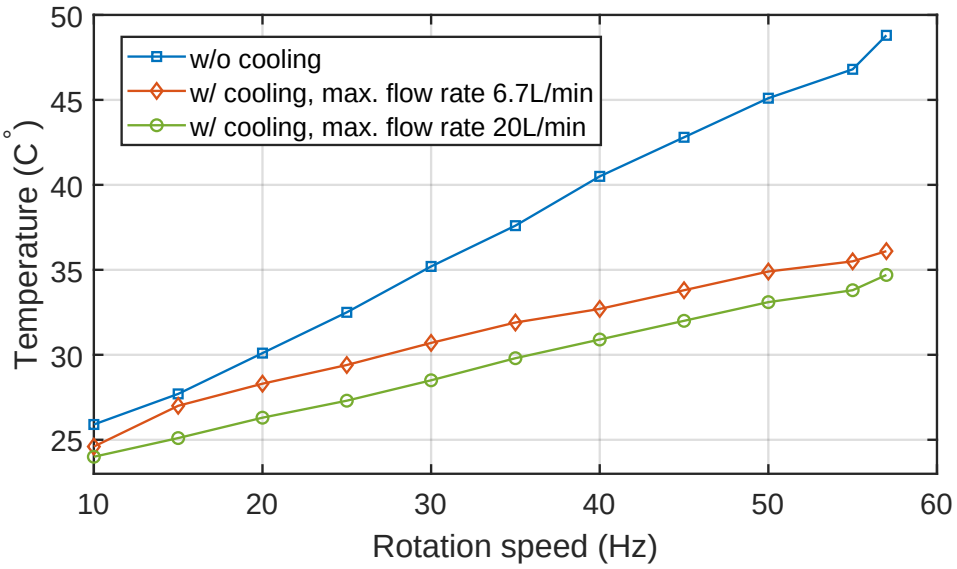

Figure B.5: The temperature measurement result after water cooling system is installed. The blue line is the same as in Fig. B.2.

C | ACS SPiiPlus Studio summary

C.1 Master-slave syntax in the controller

As the prior brief description in Sec. 3.2 stated, the syntax code is provided in Fig. C.1. Due to sufficiently high technical details which can be found in the Ref [43].

```
1    ! Axis 0 -> Rotation stage
2    ! Axis 1 -> Pulse generator
3
4    !AUTOEXEC:
5
6    ENABLE(0)
7    COMMUT (0)
8
9    !VEL0 - velocity
10   !ACC0 - acceleration
11   !DEC0 - deceleration
12   !JERK0 - jerk deg/s3
13
14   E_TYPE1=1
15   SET FPOS1=0
16   SET FPOS0=0
17
18   MASTER MPOS(0)=360*FPOS(1)
19   SLAVE/p 0
20
21   STOP
```

description/function

Line 1 : Axis is a channel where I/O communication devices take place

Line 6 : activates one or more axes

Line 7 : performs auto commutation

Line 14 : an integer array, with one element for each axis in the system, and is used for defining the encoder type

Line 15 : defines the current value of either feedback (FPOS), reference (RPOS), or axis (APOS) position

Line 18 : defines master-slave motion by creating a dependency between an axis position or velocity to a variable and/or an expression. Velocity lock is default state for MASTER.

Line 19 : initiates the motion defined by MASTER and must follow MASTER. /p means position lock or phase locked.

Figure C.1: The reproduced master-slave syntax in the ACS SPiiPlus Application Studio (left) and corresponding explanations on the right. More detail is given in Appendix C. The syntax command descriptions follow from [43].

Based on the script given in Fig. C.1, the implementation of the synchronization is relatively straightforward, yet, needs understanding to the unique controller programming language that is, unfortunately, unusual. The important feature from this master-slave syntax is that the dependency of the rotation stage, defined as axis 0, to the signal from the pulse generator through axis 1 in the controller. The coefficient 360 is the factor or "formula" in which for every signal input from the pulse generator that is read by the controller through axis 1, is converted to rotation of the rotation stage. The resulting value is defined in the unit of deg/s in the controller, i.e. frequency in Hz.

As one could also seen that several description or function has been provided in Fig. C.1, one could, particularly, focus on the syntax command from line 9 - 12. All of these syntax command is the user-manual command that can be write down in the command window

(see Fig. in the Appendix C). The more detail explanation of the user interface of the ACS SPiiPlus MMI Application Studio, MMI Apps for short, can be found in Appendix C. Moreoever, the command line in 7 is one of the command that ensure the communication between the controller and the rotation stage to receive all the commands from this syntax in the MMI Apps window.

As stated in Sec. C.1, the command window where the syntax in line 9-12 in Fig. C.1 exist, can be write down in the command window, indicated as red capital letter G in Fig. C.2. All these syntax command in line 9-12 can be manually adjusted through this command window if one want to adjust through the MMI Apps. However, one could also utilize the internal trigger from the pulse generator to have the similar effect. Practically, it was often comfortable to adjust directly from the internal trigger of the pulse generator since both of the pulse generator and the controller is already connected and synchronize with the master-slave syntax.

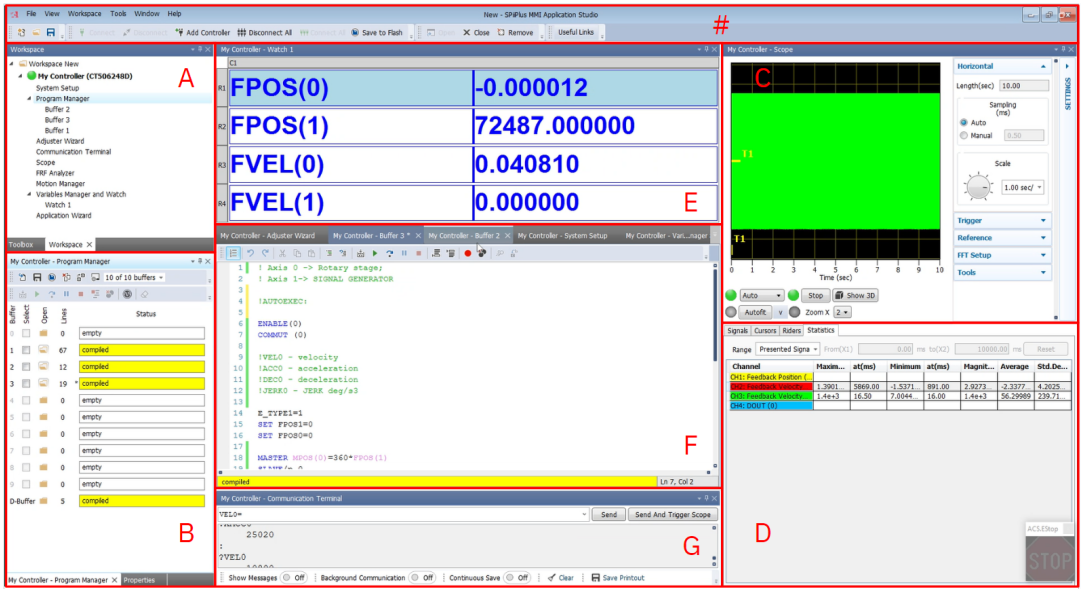

Figure C.2: The ACS SPiiPlus MMI Application Studio user interface. The main purposes of the figure is to indicate the command window and the syntax areas. Noted that the area inside the red capital letter F is the original version of the Fig. C.1 and the corresponding syntax monitor is in the area red capital letter B.

Briefly, below one could find the description of each indicated areas. The red hash tag indicates the menu bar that can be used to manage MMI Apps files, adjust the view of the overall MMI Apps, manage workspace, and related common menu bar in many application such as window and help. The area A indicates, the workspace where the interactions between user and the MMI Apps take place. The area inside the red capital letter E and C has the similar function, i.e. to monitor the synchronization through the MMI Apps. They both differs only with the representation, one inside the red capital letter E shows in numbers along with its corresponding parameters while the one inside the red capital letter C shows it as a graph with its corresponding statistical data shown in area in D, similar to the oscilloscope view.